

Characterizing the Dust and Cold-Gas Content of Nearby Star-Forming Galaxies

BY

Sean MacBride

A Study

Presented to the Faculty

of

Wheaton College

in Partial Fulfillment of the Requirements

for

Graduation with Departmental Honors

in Physics and Astronomy

Norton, Massachusetts

May 10, 2020

Abstract

Composed of baryonic and non-baryonic matter, star-forming galaxies are one of the many unique structures within the universe. Due to minimal emission contribution from their galactic core, star-forming galaxies emit similar signatures, particularly in Balmer emission. Balmer emission can be used with physical extinction processes to trace the overall composition of certain baryonic matter components within star-forming galaxies. The baryonic matter components of any galaxy can be separated into several elements: stars, gas, and dust. While accurate methods to measure the stellar component of galaxies are convenient and simple, methods to determine the dust and gas content are scant and rely on longer observations from ground and space-based telescopes. Surveys of the dust and cold-gas components exist, yet a law to describe the dust and cold-gas content as a function of Balmer emission does not currently exist. I present methods to constrain the dust and cold-gas content of star-forming galaxies using Bayesian fitting of the Balmer decrement ($\log\left(\frac{H\alpha}{H\beta}\right)$). The constraints are applied to an independent galaxy sample (SDSS) with similar physical characteristics to test the validity of the dust and cold-gas calibrations. The constraints show low intrinsic scatter, and show satisfactory results when applied to a wider star-forming galaxy sample with independent Balmer decrement measurements. The effects of inclination dependent reddening on the calibration are significant when applied to the SDSS sample, indicating the calibration requires further modification.

Acknowledgement

This project has been an arduous endeavour that has spanned continents and intergalactic space. Without the help of a few people I would not be here, and it would be a disservice to not acknowledge their contribution to this project and to my success.

Amélie Saintonge has been an unstoppable force orchestrating this project from behind the scenes. Thank you for giving me this opportunity when I walked into your office last May. This has been a challenging and rewarding experience, and I look forward to continuing this work in the future.

John Collins has been a monumental figure in my development at Wheaton College. Without your guidance and advice, I would not be in the position I am today. You have supported me from the start. I remember tinkering with lasers and q-switches in my first exposure to laboratory physics as a freshman, and I will never forget the path you helped forge for me along this strange yet fulfilling journey. I could not have asked for a better mentor over these four years, and I am so thankful for your help and direction.

Dipankar Maitra has pushed me to levels that have forced personal and academic growth beyond my expectations. You taught me to appreciate the process, and understand the rigor of every portion of it. I never realized the importance of these things until this project, and I thank you for your expertise and guidance.

I have been lucky enough to work alongside other incredible minds at Wheaton and elsewhere. During my summers outside of Wheaton, Tad Pryor of Rutgers had an enormous impact on me. Without your help and encouragement, I would not have pursued astronomy as boldly as I did.

Having such a tight network of compassionate friends, I would not have stayed sane throughout this process. Particularly, thank you Grace for tolerating my late-night rants about "roadblocks." Thank you Ian for listening to my tirades and for being supportive, even when you may not have understood everything I was saying. Kim, thanks you for helping me navigate this project and everything in-between. Mo, I don't know what I would do without such a loyal friend and associate, both inside the lab and outside the "zoo."

Thank you to my eighth-grade teachers who thought I was not smart enough to take honors classes in high school. Without that chip, I would probably not be shooting this high.

Mom and Dad, you may have never quite understood what I do every day. Despite this, you have supported me unconditionally and fully in all my endeavours. I love you so much. Thank you.

Contents

Abstract	i
Acknowledgement	ii
1 Introduction	1
1.1 The early universe and the origin of everything	3
1.2 Matter domination and the seeds of structure	5
1.3 The dark ages and the emergence of large-scale structure	7
2 Theory	10
2.1 Let there be Light	10
2.1.1 Spectroscopy	10
2.1.2 Photometry	14
2.2 Extinction	14
2.3 Dark matter's role in the growth of structure in an expanding universe	22

2.4 Galaxies	27
2.4.1 Classifications of Galaxies	29
Irregular Galaxies	29
Elliptical Galaxies	30
Lenticular Galaxies	33
Spiral Galaxies	34
2.4.2 Galactic Interactions	37
3 Calibrating Dust and Cold Gas Content	40
3.1 MCMC Methods	41
3.2 Gas mass calibrations	44
3.3 Dust mass calibrations	46
3.4 SDSS	47
4 Results	49
4.1 Sample selection	49
4.2 MCMC calibrations	51
4.2.1 Prior ranges	51
4.2.2 LCO ₁₋₀	52

4.2.3	Gas Mass	58
4.2.4	Dust Mass	62
4.2.5	MCMC results	66
4.3	Applying the Calibration: SDSS	66
4.3.1	Molecular gas	68
	Gas Fraction	70
4.3.2	Dust Mass	71
5	Conclusion	74

Chapter 1

Introduction

The beginning of time was a bang, a long time ago. The event known as the big bang occurred 13.7 billion years ago when a very small, hot, and dense conglomeration of matter expanded from an infinitesimally tiny size to the universe we know today. From this minuscule singularity, galaxies, gas clouds, stars, planets, and life emerged. Each of these important entities were formed in different processes that required certain conditions to be met. These structural processes are driven by the evolution of the universe on a macroscopic scale. To understand the development of any one of these complex structures, an understanding of the evolution of the environment hosting these structures is necessary.

A forewarning: the theory of the universe's origin, development, and ultimate fate is up to personal interpretation based on belief. While it may be tempting to believe in the interference of a higher being pulling the strings, the scientific basis of what follows is firmly grounded in the Copernican principle. Named in honor one of the grandfathers of astronomy Nicolaus Copernicus, it confines humans to being unexceptional observers of the universe. We do not occupy a special location in ei-

ther space or time within the universe. While this concept may seem novel, it allows astronomers and astrophysicists to make conclusions about the universe as a whole. The Copernican principle is the floor we stand upon. From this floor, I would like to tell you a story.

The model that best explains many features of the universe on a grand scale is called the Λ CDM model of cosmology(1). The Λ CDM model assumes four principal components that were influential to grand-scale evolution: electromagnetic radiation, baryonic matter, dark matter, and dark energy. Each component was integral to the evolution of the universe at different epochs within its evolution.

There are four fundamental forces in the present day universe that can interact with matter(2). The weakest of these forces is the one that is the most important on large scales, the gravitational force. Gravity is unique in its ability to act on an infinite range with an attractive force between any and all matter with mass within the universe. Slightly stronger than gravity is the weak force. In contrast to gravity, the weak force acts only on leptons and quarks on small scales ($\sim 10^{-18}$ m) in order to mediate particle decay. It is not a repulsive or attractive force; it changes the flavor of certain subatomic particles. This effect is paramount to radioactive decay and nuclear fusion within stars. The electromagnetic force is stronger than the weak force, and acts upon all electrically charged matter. It is similar to gravity in that it has an infinite range, but unique in that it can be both attractive and repulsive. Electricity, magnetism, and light are phenomena produced by the electromagnetic force. The strongest of these forces is unsurprisingly, the strong force. It acts on relatively small scales ($\sim 10^{-15}$ m) to hold atomic nuclei together to overcome the repulsive electromagnetic force of nearby protons.

These four forces each played important roles in the evolution of the universe over

the past 13.7 billion years. Over this time, structure has emerged from a chaotic and turbulent origin. The physical evolution of structure within the universe can be loosely defined within three stages.

1.1 The early universe and the origin of everything

As cosmic time convened, the conditions were so extreme that the only way to explain the phenomena that followed is theory(3). The prevailing theory predicts energy scales that cannot currently be probed on earth with the most powerful particle accelerators. Consequently, the primordial universe is poorly understood. However, it is agreed upon that the initial conditions of the universe were inconceivably dense, homogeneous, and hot.

Physics begins to explain the dynamics of the early universe following the Planck epoch, $\sim 10^{-43}$ s after the big bang. Before the Planck epoch, the temperature and energy of the universe was so great that subatomic particles could not form, and current physics can not describe the universe. In order to explain the events that occurred in this brief yet important time period, union between quantum mechanics and the theory of gravity is required. After the Planck era, the laws of quantum mechanics began to govern the universe.

For a brief period of time after the Planck epoch, the average temperature and energy was so high that the four fundamental forces of the universe were merged in one unified force. As the universe cooled, gravity split from the other unified forces. The universe further cooled to allow for the strong force to separate from the electroweak force, before the electromagnetic force separated from the weak force.

At $\sim 10^{-36}$ s after the big bang, the universe began a period of rapid expansion in

space. During this time the linear size of the universe expanded by an order of $\sim 10^{26}$. An analogous comparison to the expansion would be the amplification of something the width of a human hair to the diameter of the Milky Way. This rapid expansion is referred to as cosmic inflation. Despite having a wealth of evidence for cosmic inflation, it is still unknown what physical mechanism caused it to occur. One piece of experimental evidence supporting cosmic inflation is you, the reader. Despite homogeneity in the universe globally before inflation, small fluctuations in matter existed on quantum scales. During inflation, these small overdensities were expanded to massive scales. These slight imperfections in matter-density uniformity within the early universe planted the seeds for structure to form in the eons to follow.

The effects of cosmic inflation are believed to have occurred $\sim 10^{-36} - 10^{-32}$ s after the big bang, but it is not the only period where the universe was expanding in size. The universe will (probably) always be expanding. As a result of expansion, the universe cooled. This allowed for more complex particle interactions to occur. One of which was baryogenesis, which brought the advent of baryons. This occurred after the end of cosmic inflation, where an unknown reaction at extremely high energy must have occurred in order to create an excess of matter over antimatter(4).

The universe continued to expand, and at $\sim 10^{-11}$ s it cooled to typical energy levels that can be probed by particle accelerators here on earth. As a result, the evolution of the universe is far better understood past this time. At $\sim 10^{-6}$ s, the universe had cooled to allow formation of free protons and neutrons. Then, ~ 2 minutes after the big bang, a small fraction of the free particles combined into light atomic nuclei during a period called nucleosynthesis.

1.2 Matter domination and the seeds of structure

After nucleosynthesis, not a lot happened for $\sim 47,000$ years. The expansion of the universe was driven by electromagnetic radiation from photons and neutrinos(3), which dominated the energy-density budget of the universe at this time. After $\sim 47,000$ years, the universe's large scale dynamics were driven instead by non-relativistic atomic nuclei: baryons. The attractive force between baryons was driven by gravity, and the rate of expansion was slowed during this time.

Despite baryonic matter dominating the large scale evolution of the universe at this time, it was actually the non-baryonic counterpart dark matter that laid the foundation for structure of any kind to emerge in the years to follow(5). Dark matter does not emit or absorb any form of radiation, in contrast to baryonic matter which emits radiation in the form of blackbody radiation spectrum (equation 2.1). Despite not emitting electromagnetic radiation, dark matter still interacts gravitationally - it has mass, yet it is collisionless with baryonic matter. The gravitational interaction between both baryonic and dark matter meant that both matter components felt an attractive force to collapse upon themselves. However, the emission of radiation from baryonic matter also meant that baryons exerted a radiation pressure from their photons, which were coupled to them at this time. This radiation pressure prevented baryonic matter from collapsing as rapidly as dark matter. As a result, the quantum irregularities that were amplified during cosmic inflation were augmented further by the collapse of dark matter into diffuse structures before baryonic matter. This process was essential to the formation of structure in the universe.

The universe continued to cool, as it always has and likely always will. $\sim 370,000$ years after the big bang, another important evolutionary step began. The hot ionized plasma that had occupied the universe since the beginning of time had cooled to

the point that electrons were not immediately ionized upon capture by a proton or helium nucleus. This process is called recombination, and it resulted in the transformation from ionized to neutral particles, mainly hydrogen and helium(6). Electrons were more efficiently captured at high energy levels, and in relaxing to lower energy states the nuclei emitted photons. This release of photons was called photon decoupling. The physical effect of this decoupling removed the photons exerting a radiation pressure that prevented the collapse of baryonic overdensities. This allowed for the beginning of formation of baryonic structure. Most of the emitted photons from the electron capture could now travel freely along long distances due to the tremendous abundance of neutral particles. This is observed as the cosmic-microwave background today as temperature fluctuations, and is the most distant remnant from the earliest era of the universe.

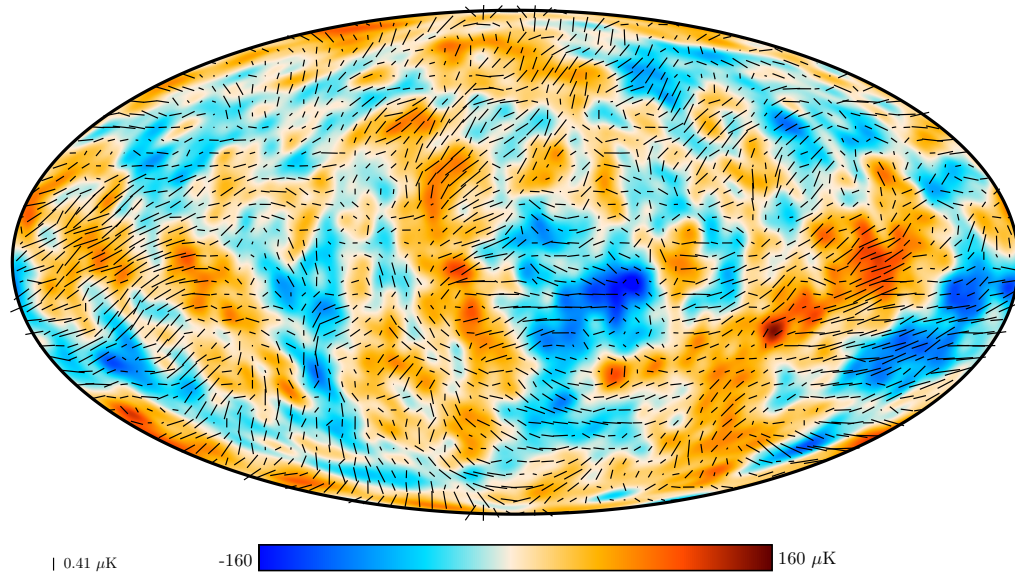


Figure 1.1 The 2018 Planck map of the polarized CMB anisotropies, shown as rods whose direction and length represent the direction and amplitude of polarized CMB. The colored background is the map of intensity anisotropies, smoothed to 5 degrees (1). Simply put, this is a map of the earliest light we can observe.

1.3 The dark ages and the emergence of large-scale structure

As the universe transitioned from an ionized soup of particles to become transparent and neutral, there were initially no light-emitting objects in the universe. The only photons in the universe were remnants from recombination and light emitted from a spin flip transition in neutral hydrogen, which is an incredibly rare circumstance. This period was called the dark ages. Despite darkness, gravitational collapse of matter continued to occur, which led to the first stars. The formation of stars that emitted ionizing radiation spurred the end of the dark ages.

As the earliest stars began to form from collapsing clouds of gas, the seeds of structure planted from cosmic inflation finally begin to bear baryonic fruit. Based on observations, the earliest galaxies formed approximately 400 million years after the big bang(7). The prevailing theory of galaxy formation is that they formed from the "bottom up", with large gas clouds collapsing to form stars before the stars clustered to develop the more intricate structure of galaxies. Further discussion of galaxy formation is found in 2.4.1, but the central formation mechanism of galaxies is the collapse of (mostly) hydrogen clouds to form stars in clusters, before the clusters merge to form the galaxies we see today(8). This process takes a tremendous amount of time, and theory can only be compared to observations using computer simulation.

Stars and gas are not the only component in present day galaxies. Interstellar dust is another component. Collisions of neutral atoms can accrete to form larger dust grains(9). This process can only occur in dense regions between stars, known as the interstellar medium (ISM). Additionally, interstellar dust can be produced in the ejecta of core-collapse supernovae from massive stars and within the gaseous outflows from

stars known as stellar winds. Dust can also be destroyed in a variety of mechanisms including sublimation, photoejection, sputtering, and grain-grain collisions.

Stars, gas, and dust compose the baryonic matter budget of a typical galaxy. In an effort to gain knowledge of the evolution of baryonic structure within the universe, an understanding of how each matter component evolved is necessary. In star-forming galaxies, there exists a large reservoir of hydrogen gas to form stars. Due to the higher rates of newborn stars, there also exists a tremendous amount of ionizing radiation. This ionizing radiation induces continuous hydrogen line emission from gas, particularly in the Balmer series. The Balmer series emits light in electronic transitions from $n > 2 \rightarrow n = 2$. The two most prominent spectral lines are $H\alpha$ and $H\beta$, which are transitions from $n = 3 \rightarrow n = 2$ and $n = 4 \rightarrow n = 2$ respectively. In the gaseous environments where spectral lines are produced, the intensities of the lines depend on several factors. These factors include gas temperature, gas density, and chemical composition. The effects of extinction are wavelength dependent, meaning that different Balmer emission lines are extinguished by different amounts depending on the wavelength. Gas and dust are the primary mechanisms for extinction of light on galactic scales. The line fluxes of $H\alpha$ and $H\beta$ can be compared using the Balmer decrement, $\log\left(\frac{H\alpha}{H\beta}\right)$. The Balmer decrement is altered by gas and dust through extinction, as extinction affects each spectral line differently.

I provide constraints on the dust and molecular gas content in star-forming galaxies. In section 2 I give a broad overview of the physical mechanisms that effect the light received from galaxies, galaxy properties, as well as the formation processes of non-baryonic structure that give rise to baryonic structure. In section 3 I provide a full explanation of the methods used to obtain and improve the quality of data before algorithmically finding relationships between unknown parameters. These relationships are presented and discussed in detail in section 4. The conclusions and applications

of this study along with explanation of how these results can be leveraged for more powerful insights into the matter functions of galaxies is included in section 5.

Chapter 2

Theory

2.1 Let there be Light

The physical entity that astronomical analysis originates from is light in the form of photons. Photons are an elementary particle that exhibits properties of both waves and particles. The wave-like properties can be manipulated through diffraction and interference to analyze the individual wavelengths of light, while the particle nature of photons allows for the analysis of the total amount of light collected from a source. These two methods of analysis are called spectroscopy and photometry.

2.1.1 Spectroscopy

Photons emitted from objects in thermal equilibrium are emitted in a range of light, called a spectrum. The shape of the spectrum, called blackbody radiation is generally

described by Planck's law(10).

$$B_\nu(\nu, T) = \frac{2h\nu^3}{c^2} \frac{1}{e^{\frac{h\nu}{k_B T}} - 1} \quad (2.1)$$

where $B_\nu \equiv$ the amount of spectral energy emitted from a blackbody at temperature T , $k_B \equiv$ the Boltzmann constant. and $h \equiv$ the Planck constant. Stars are not perfect blackbodies, but they are very close. As a result, they emit starlight in a blackbody-like shape. Spectra are obtained using an instrument called a spectrometer.

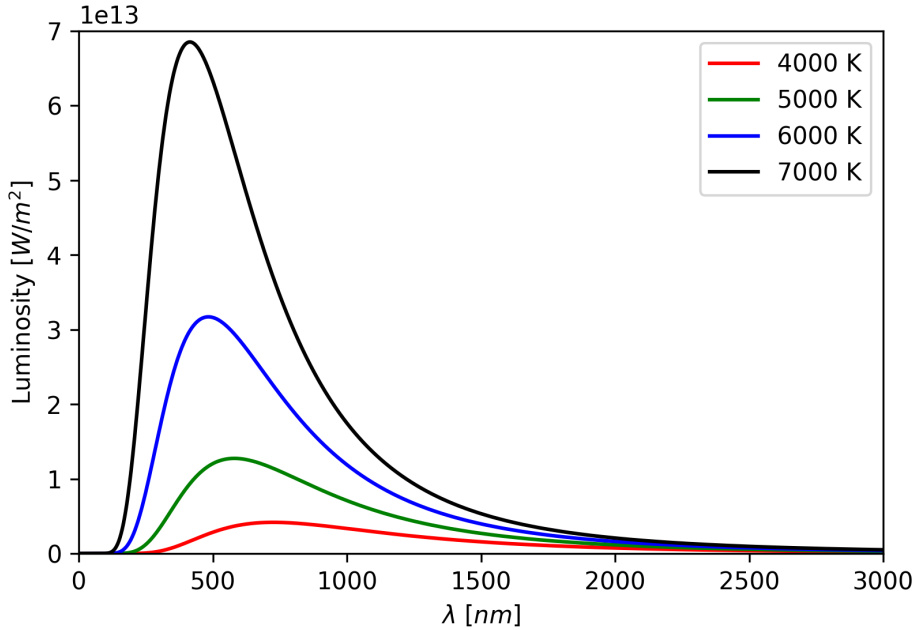


Figure 2.1 Luminosity of light emitted at different wavelengths from a blackbody at different temperatures according to Planck's Law (2.1).

The spectrum emitted by a perfect blackbody as white light is described by figure 2.1 and is called a continuous spectrum. The spectrum is a smooth, continuous function. Real spectra are modulated based on the intervening material between the source and a detector.

If light received by a detector passes through a cool gas before measurement by a

spectrometer, the observed spectrum is called an absorption spectrum. An absorption spectrum is a continuous spectrum of light with lower intensities at wavelengths corresponding to the energy levels of the intervening cool gas. This appears as dark lines across the continuum. When a gas absorbs energy from light, it re-emits that light in all directions. This results in an emission spectrum of the gas, appearing as light at discrete wavelengths and specific energy levels of the gas(11). This appears on a spectrum as lines of light at different frequencies with their intensity correlating with the population of that particular energy level transition. The absorption and emission lines apparent in spectra correspond to the element specific electronic transition of the gas.

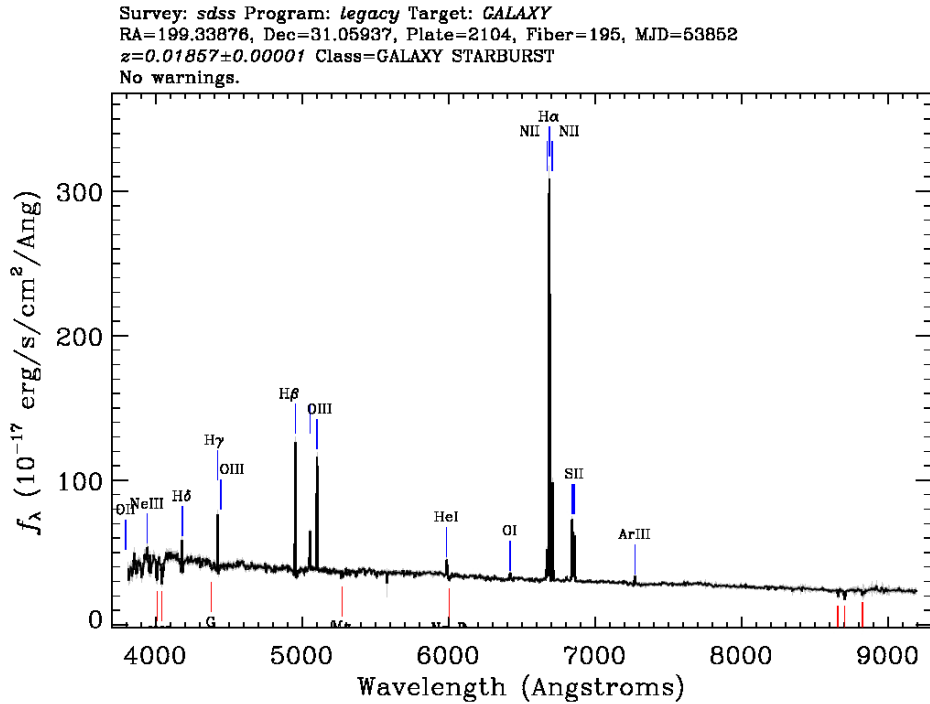


Figure 2.2 Spectra of the galaxy J131721.28+310334.1 obtained using SDSS DR-16. This galaxy is a star forming galaxy at $Z = 0.019$ and is a member of the JINGLE survey. This spectrum is of an older galaxy of the galaxies within this survey. Absorption (blue) and emission (red) from elements are labeled within the spectrum.

The spectra in figure 2.2 features H α as the most prominent emission line. This is

the transition from $n = 3 \rightarrow n = 2$, and it is an important focus of this study. Any transition in the hydrogen atom from $n_i > 2 \rightarrow n = 2$ is a Balmer series transition. Deriving the relative intensity for $H\alpha$ and other emission lines comes from the Boltzmann distribution, which describes the population density n_i of an energy level E_i of a classical gas with N accessible states and a degeneracy g_i in thermal equilibrium at temperature T . A is a normalization factor to account for the sum of probabilities of possible states to equal 1.

$$n_i = A^{-1} g_i e^{-\frac{E_i}{k_B T}} = \frac{g_i e^{-\frac{E_i}{k_B T}}}{\sum_{i=1}^N e^{-\frac{E_i}{k_B T}}} \quad (2.2)$$

While equation 2.2 describes the population states of a classical gas, it does not account for the fraction of ionized electrons in a gas. When gases become hot or dense enough, the atomic collisions will ionize the gas. The Saha equation describes the degree of ionization for a gas in thermal equilibrium at temperature T .

$$\frac{n_{i+1} n_e}{n_i} = \frac{G_{i+1} g_e}{G_i} \frac{(2\pi m_e k_b T)^{3/2}}{h^3} e^{-\frac{\chi_i}{k_b T}} \quad (2.3)$$

n_i represents the number density of the i th ionization state, G_i is the partition function of the i th state, and χ_i is the ionization potential from state i to $i + 1$. n_e represents the electron density, g_e represents the degeneracy of an electron ($g_e = 2$), and m_e equals the mass of the electron. For hydrogen, under most astrophysical conditions, $G_i \approx 2$ and $G_{i+1} \approx 1(12)$.

Balmer emission spectra can be observed in a wide array of astronomical objects, due to the overwhelming abundance of hydrogen within the universe. They can be used as a standard ruler to make sweeping assumptions about the large scale universe as a whole. Applying the effects of the physical environment on this spectral feature can

provide insight into intriguing characteristics of the environment.

2.1.2 Photometry

Photometry utilizes the overall intensity of or flux light received from objects using a photometer. With modern technology, photometry is performed by converting light into electric current by the photoelectric effect. Coupling photometry with the use of optical filters allows for comparative analysis over different wavelength bands. Coupling photometric and spectroscopic methods allows for the creation of a spectral distribution of the intensity of light received at specific wavelengths.

A useful way of obtaining photometry on astronomical objects is with a grid of detectors, called a CCD camera. Using a grid of detectors, it is possible to obtain data from all objects within the field of view.

2.2 Extinction

Equations 2.1 and 2.3 are based on the broad assumption that photons do not interact with any matter after they are emitted. In reality, photons interact with their surroundings in a several ways. Light emitted from a distant object can be scattered and absorbed by gas and dust along the line of sight of the object. The effect of physical interactions of dust and gas on light is called extinction.

Extinction has two primary effects on the spectra of light as a result of the two physical interactions that drive extinction. Absorption of light by interstellar gas and dust result in absorption features in the spectrum from a source. Absorption features can give insight to the chemical composition of the intervening interstellar

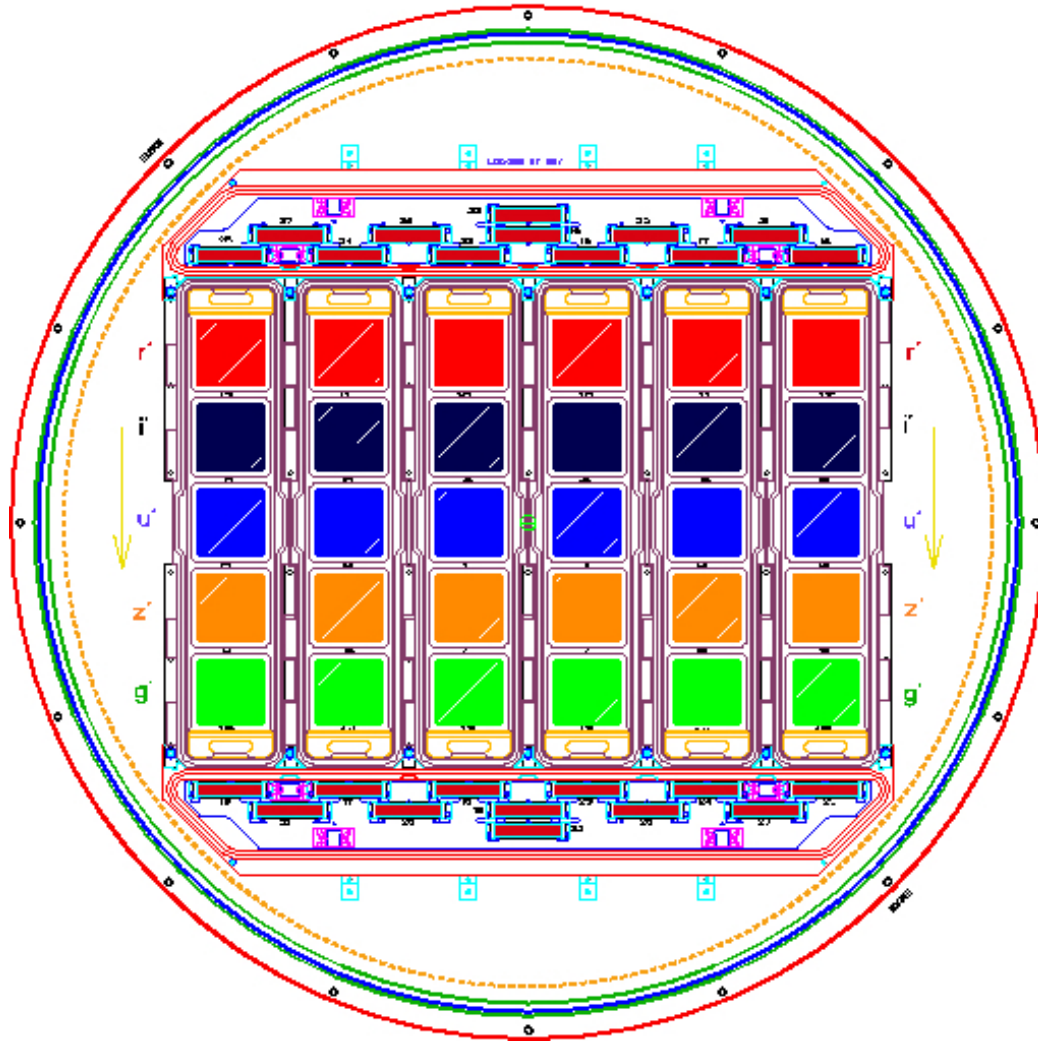


Figure 2.3 Schematic of the CCD camera used by the Sloan digital sky survey (SDSS)(13).

material. The scattering of light off of interstellar material results in the attenuation of light according to its frequency. Blue light is more energetic, and is more strongly diminished than red, less energetic light. This results in extincted objects appearing redder than expected, a process called interstellar reddening.

Early evidence for the effects of dust and gas on light first came from infrared observations of dark clouds(15). Dark clouds are dense clouds of gas and dust that obscure almost all visible light of background objects. Observations of lower energetic light in infrared, microwave, and radio frequencies illuminate objects both within and behind

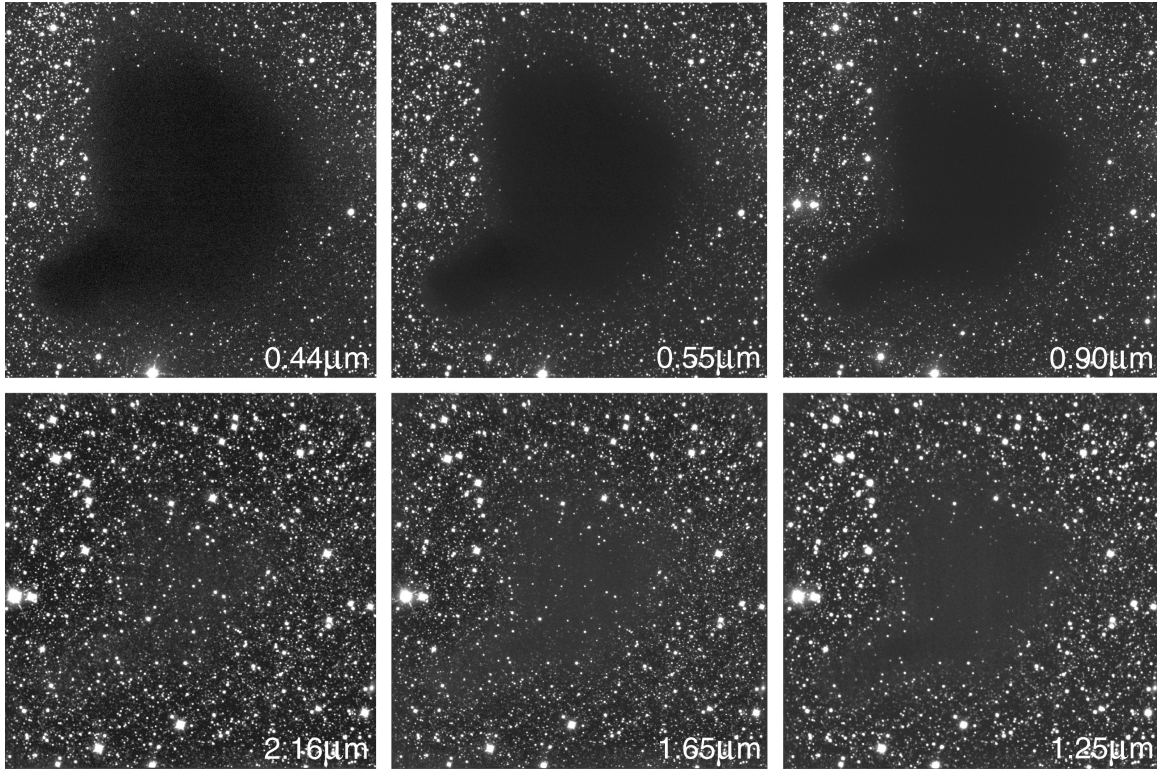


Figure 2.4 Composite images of Barnard-68. Barnard-68 is a dense molecular cloud within the milky way made of dense, cold gas and dust. The cloud is opaque at visible wavelengths, but is shielding over 1,000 background Milky Way stars which can be observed in the infrared(14).

these clouds. Dark clouds were the first objects to hint towards conclusions on the ways interstellar dust and gas affect light of different wavelengths. Scattering processes are the most efficient when the wavelength of light is comparable to the size of the extinguishing component.

Understanding how extinction affects light of different wavelengths could provide more precise analysis of spectroscopic data. Empirical prescriptions to describe how light is suppressed by absorption and scattering processes with interstellar material on a galactic scale show that the amount of extinction is proportional to the energy of the emitted light(16).

In star-forming galaxies there exists a tremendous reservoir of hydrogen gas. Hy-

hydrogen line emission is therefore a dominant feature of the spectra obtained from galaxies. The two dominant spectral lines within the visible wavelength range are Balmer series transitions $H\alpha$ and $H\beta$. $H\alpha$ has a transition energy of $1.89eV$, while $H\beta$ has a transition energy of $2.55eV$. When comparing ratios of these spectral lines in different sources, inferences on the amount of extinction can be made by observing the light obtained by a distant luminous source with gas and dust.

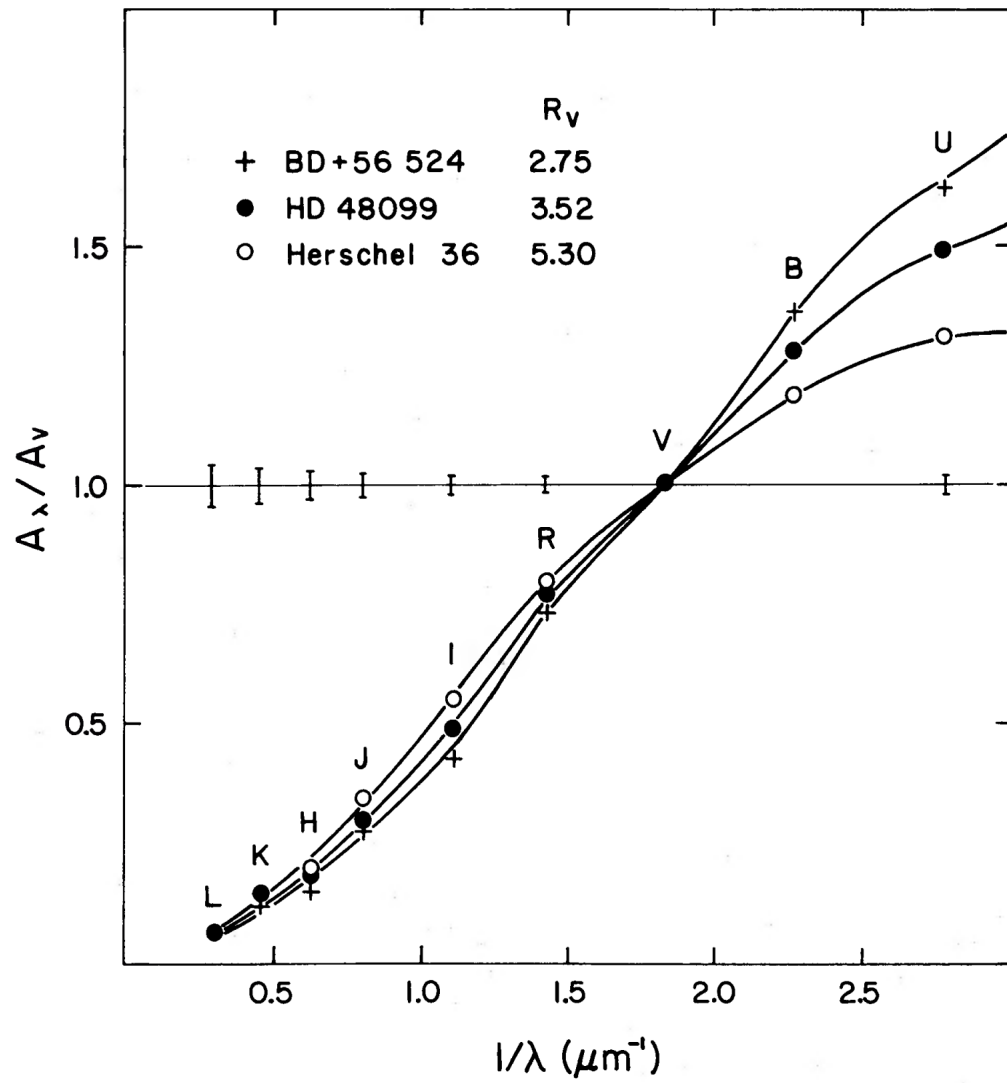


Figure 2.5 The wavelength-dependent relationship between absolute extinction $\frac{A(\lambda)}{A(V)}$ of visible and near infrared light. Observational evidence indicates extinction processes are more efficient on higher energy light(16).

Several parameters are involved in empirical analysis of extinction. Extinction is expressed in terms of magnitudes, and is a function of the wavelength. Observed magnitude $m(\lambda)$ of a source can be expressed by

$$m(\lambda) = m_0(\lambda) + A(\lambda) \quad (2.4)$$

where $m_0(\lambda)$ is the magnitude at the wavelength λ observed in the absence of extinction $A(\lambda)$. A standard metric of extinction is the color index of an object, $E(B - V)$. This quantity is derived by taking the difference of extinctions at $\lambda_V = 550nm$ and $\lambda_B = 440nm$.

$$E(B - V) = A(B) - A(V) = (m(\lambda_B) - m_0(\lambda_B)) - ((m(\lambda_V) - m_0(\lambda_V))) \quad (2.5)$$

$E(B - V)$ is also referred to as selective extinction, as it gives a relationship between extinctions at different wavelengths. The total extinction at any wavelength is found by extrapolating the extinction curve (figure 2.5). Assuming $A(\lambda) \rightarrow 0$ as $\lambda \rightarrow \infty$. The intercept on the y-axis gives the ratio of total to selective extinction, R_V .

$$R_V = \frac{A_V}{E(B - V)} \quad (2.6)$$

$R_V = 3.1$ for diffuse clouds(17), but can vary based on the type of environment observed.

To study how extinction can affect Hydrogen emission line flux, called the Balmer decrement ($\log\left(\frac{H_\alpha}{H_\beta}\right)$), consider how a range of values of R_V and $E(B - V)$ could impact the Balmer decrement of a source. Adopting an intrinsic Balmer decrement of $BD_0 = \frac{F_{H_\alpha}}{F_{H_\beta}} = 2.86$ (18), the observed magnitude of a source can be rewritten in

terms of the extinction of the source.

$$A_\lambda = -2.5 \log \left(\frac{F_\lambda}{F_{\lambda,0}} \right) \quad (2.7)$$

Inserting the appropriate fluxes for $H\alpha$ and $H\beta$ yields

$$\frac{H_\alpha}{H_\beta} = BD = BD_0 10^{-0.4(A_\alpha - A_\beta)} \quad (2.8)$$

Applying the prescription described by Cardelli Clayton and Mathis(16) gives $\frac{A_\lambda}{A_V}$. In applying this prescription, the additional A_V factor must be accounted for. Therefore, rewriting equation 2.6 gives

$$BD = BD_0 10^{-0.4 \times A_V \times \left(\frac{A_\alpha - A_\beta}{A_V} \right)} = BD_0 10^{-0.4 \times E(B-V) \times R_V \times \left(\frac{A_\alpha - A_\beta}{A_V} \right)} \quad (2.9)$$

This relationship coupled with the formulae provided by Cardelli Clayton and Mathis's(16) results provide an empirical method to represent the effects of extinction on the Balmer decrement from a source.

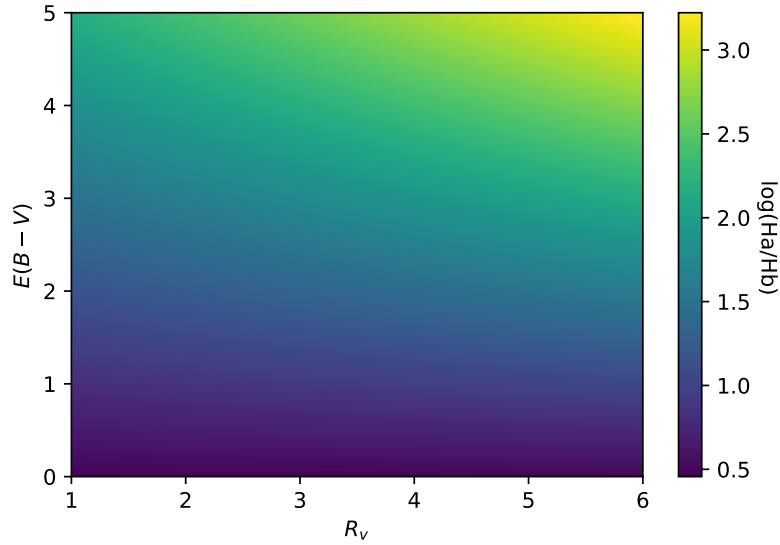


Figure 2.6 A colormap showing how R_V and $E(B - V)$ affect the balmer decrement of a source. As $\lambda_\alpha(656.56nm) > \lambda_\beta(486.13nm) \rightarrow E \propto \frac{1}{\lambda}$, therefore $E_\alpha < E_\beta$ & $A_\alpha < A_\beta$. This functional relationship means $\frac{H\alpha}{H\beta}$ will be higher in environments with higher extinction.

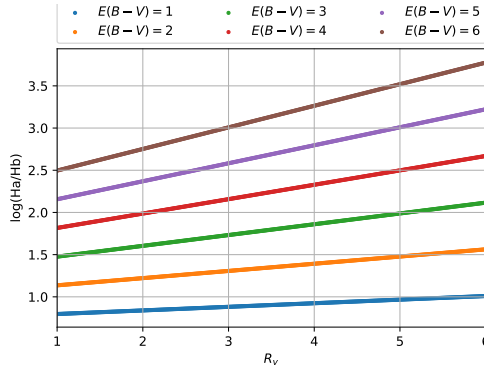


Figure 2.7 Applying equation 2.9 for fixed values of $E(B - V)$ and allowing R_V to vary continuously shows that higher values of $E(B - V)$ results in higher values of $\frac{H\alpha}{H\beta}$

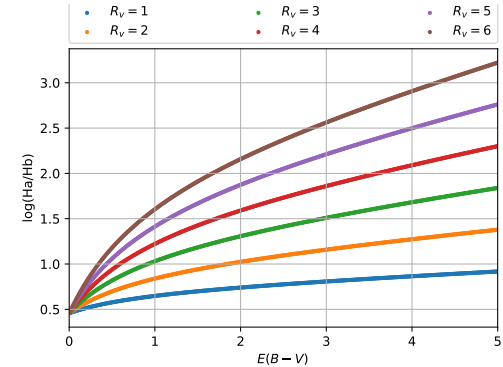


Figure 2.8 Applying equation 2.9 for fixed values of R_V and allowing $E(B - V)$ to vary continuously shows that higher values of R_V result in higher values of $\frac{H\alpha}{H\beta}$

The results in figures 2.6, 2.7, and 2.8 are based on a value of $BD_0 = 2.86(18)$, which is a reference for gaseous nebulae. While the focus of this study is galaxies and not diffuse nebulae, it serves to probe the functional relationship between extinction and

its effect on observations.

The neutral interstellar hydrogen column density within the Milky way has been found to be a mean value scaled by the color excess $E(B - V)$ of the source(19).

$$\langle N(HI + H_2)/E(B - V) \rangle = 5.8 \times 10^{21} \text{ atoms cm}^{-2} \text{ mag}^{-1} \quad (2.10)$$

To convert the number density to the total hydrogen mass, the mass of hydrogen m_H is introduced. To account for the magnitude dependency, the color excess $E(B - V)$ can reduce equation 2.10 to

$$M(HI + H_2) = E(B - V) \times m_H \times 5.8 \times 10^{21} \text{ cm}^{-2} \quad (2.11)$$

with $m_H = 1.673 \times 10^{-27} \text{ kg}$. I am motivated to find the interstellar neutral hydrogen content as a function of color excess $E(B - V)$, the distance to the source D , and the angular area a the source occupies on the sky.

For an object that is at a distance D and occupies an angular area a , the physical area A the object occupies is $A = aD^2$. To account for the area dependencies of equation 2.11, these results can be scaled by $F \times a \times D^2$ where F is a correction factor determined by $a = 1$ and $D = 1$. If we select units of D in megaparsec, and units of a in square arcseconds, A becomes

$$F = aD^2 = 1 \text{ arcsec}^2 \left(\frac{1\text{deg}}{3600\text{arcsec}} \frac{\pi\text{rad}}{180\text{deg}} \right)^2 (1\text{Mpc})^2 \left(\frac{3.086 \times 10^{24}\text{cm}}{1\text{Mpc}} \right)^2 \quad (2.12)$$

$$F = 2.238 \times 10^{38} \text{ cm}^2$$

The full form of equation 2.11 to include the scaling of distance and angular area is

$$M(HI + H_2) = a \times D^2 \times E(B - V) \times 2.172 \times 10^{-27} [\text{kg}] \quad (2.13)$$

with D [Mpc], a [arcsec 2], and m_H [kg]. This equation can predict neutral hydrogen mass of an object as a function of angular area, distance, and color excess.

Illustrated in equation 2.13, the effect of extinction on a light source can be used to infer the environment around the source. Interstellar dust is a particularly efficient vehicle for extinguishing starlight. A broad takeaway from extinction surveys (16)(20) is the efficiency and randomness of the process as a whole. This suggests that the effects of extinction are efficient and occur on a universal scale.

While the derivations in equations 2.9 and 2.13 are based on interstellar observations, the universal physical process of extinction suggests that similar laws exist on intergalactic scales. Therefore, the same method could be followed for intergalactic observations, as equations 2.9 and 2.13 are unlikely to be entirely correct. Column density distributions have been found for the inter-galactic medium on intermediate redshifts ($\langle Z \rangle = 2.37$)(21), but general relations over the redshift range of this study ($0 < Z \leq 0.06$) do not currently exist.

2.3 Dark matter's role in the growth of structure in an expanding universe

The observable universe is full of rich structure. Georges Lemaître was a French pioneer in cosmology who eloquently described that "the evolution of the world can be compared to a display of fireworks that has just ended: some few red wisps, ashes

and smoke. Standing on a well-chilled cinder, we see the slow fading of the suns, and we try to recall the vanished brilliance of the origin of the worlds." The origin of worlds can be viewed through the ingredients required to construct them. The primary ingredient that derived the structure we observe today is dark matter. Dark matter accounts for $\sim 85\%$ of the matter within the universe. The presence of dark matter is lurking within other observational signatures we observe in the rich structure of the universe today.

In 1933, Fritz Zwicky was investigating galaxy clusters, and found discrepancies in the total mass that led to the first observational evidence of dark matter(22). Zwicky estimated the mass of the cluster through gravitational methods, and he found an unexplained excess of mass when compared to photometric methods of obtaining the cluster mass.

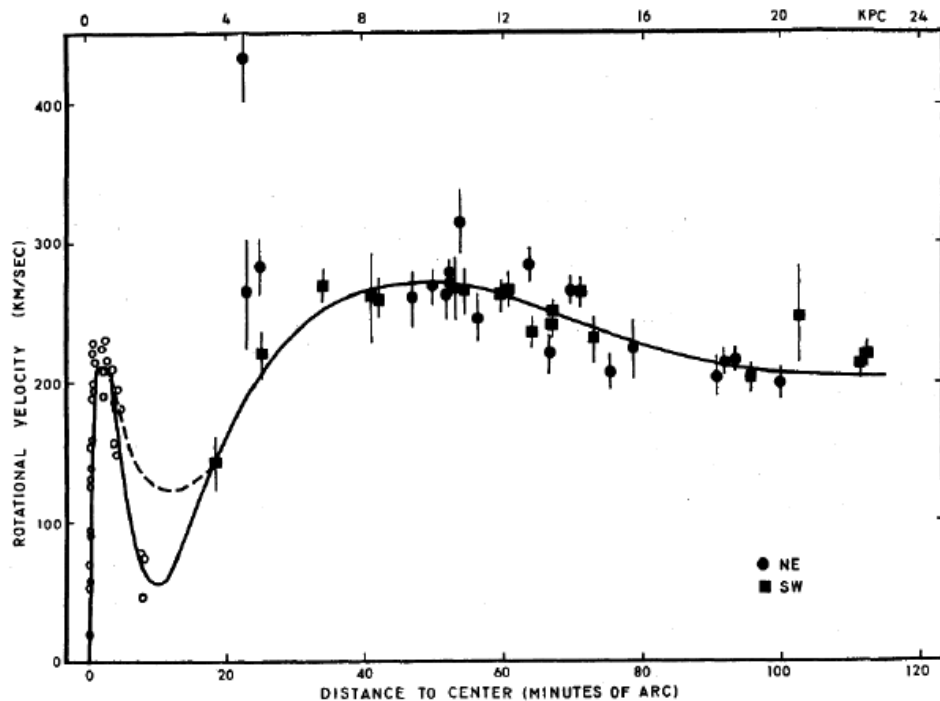


Figure 2.9 Rotation curve of the Andromeda galaxy obtained using an image tube spectrograph by Vera Rubin and Kent Ford(23). This result was in direct contrast to the expected rotation curve of a galaxy which should decrease $\propto \frac{1}{r^2}$ if the galactic disk were the only mass component at large radii.

Dark matter differs from baryonic matter in its electromagnetic signature. While sources of baryonic matter can be traced using photons, dark matter emits no photons. Its existence can be inferred not from the direct measurement of it, but by the effects it has on other objects. Another landmark investigation into dark matter came from Vera Rubin’s studies of the peculiar velocities of spiral galaxies at different distances from their center(23). She found that large distances, the matter in the galactic disk could not be the only matter constituent driving the motion of the galaxy. Rubin concluded that in order for a galaxy to remain stable and not tear itself apart, some sort of matter must exist in tremendous abundance. Rubin’s results were the first observational evidence suggesting that galaxies contain (by conservative estimates) less than 50% of their mass within the luminous disk.

Evidence for dark matter is not confined to galaxies. Observations of interacting clusters of galaxies also show evidence for an excess of collisionless mass. The bullet cluster is the most famous example of cluster interaction with evidence for dark matter within the cluster.

Figure 2.10 shows the bullet cluster, with the gas and total mass of each cluster represented with different colors. The gas from each cluster has been clearly displaced, with one cloud showing signs of a bow shock from the collision. As most of the matter in the cluster is collisionless dark matter, both galaxy clusters and their galaxies still retain their structure. The preservation of this structure is very strong evidence for the existence of collisionless dark matter.

Observational evidence for dark matter in the luminous structure of the universe would imply that it plays an integral role in the formation of the structure of the universe. This can be traced to the earliest consequences of cosmic inflation. Before cosmic inflation ($\sim 10^{-36}s$ after the big bang), the universe was homogenous and

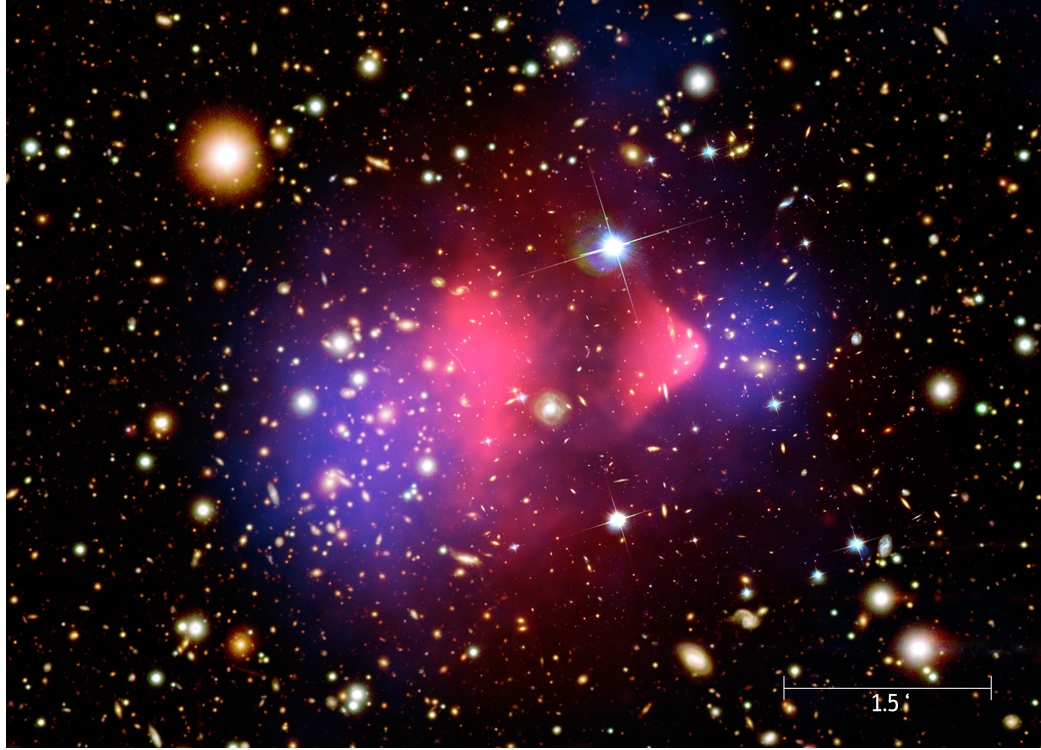


Figure 2.10 The bullet cluster, shown with X-ray flux from baryonic gas content in pink, and the total matter density reconstructed from weak gravitational lensing(24)

isotropic in a thermodynamic sense. On quantum scales, fluctuations in all matter and energy were amplified to gargantuan scales as a consequence of inflation(25).

The growth of matter overdensities spawned from inflation depended on the nature of the overdensity, the scale of the overdensity, and the state of the central component driving the evolution of the universe.

The central dependencies of matter overdensity growth also give rise to three important junctures in time. There are two fixed points in the history of the universe: the time of the matter-radiation equality ($\sim 50,000$ years after the big bang) and the time of recombination ($\sim 370,000$ years after the big bang). The third influential event in overdensity growth has to do with the time that the size of the overdensity is comparable to the size of the observable universe, known as the hubble radius, $R_H = \frac{H(t)}{c}$ ($H(t)$ denotes the Hubble constant as a function of time t and c denotes

the speed of light). The time of an overdensity entering the horizon depends on the size of the overdensity, and can occur before the matter-radiation equality, before recombination, or even after recombination. As the overdensity grows, it decreases in linear size. The growth of structure evolves as follows.

While matter overdensities are larger than the apparent horizon of the universe, they grow. The rate of growth is slightly higher in radiation domination than in matter-domination. As the size of the overdensity decreases and the universe expands, it eventually becomes small enough to enter the horizon of the universe. Several things can happen at this point based on the state of the universe at this time.

If the matter overdensity enters the horizon before the matter-radiation equality, it does not grow(26). At the time of the matter-radiation equality, the dark matter component of the overdensity begins to grow. The baryonic matter component is still coupled to photons at this time, which prevents the growth of overdensities through radiation pressure. Signatures of this interaction can be observed in the power spectrum of matter, known as baryonic acoustic oscillations (BAO's)(27).

If the matter overdensity enters the horizon after the matter-radiation equality but before recombination, the dark matter component of the overdensity begins to grow while the baryonic component is stagnant. The physical BAO interaction is the same process preventing the collapse of baryonic matter.

Recombination occurs after the matter-radiation equality, and results in the decoupling of photons from baryonic matter. With a lack of radiation pressure to prevent collapse, gravity takes control of baryonic collapse. The dark matter overdensities that grew from the start of the matter-radiation equality accelerate the growth of baryonic overdensities at this time(28).

Dark matter was a seed to the plants that we observe today in galaxies. Dark matter collapsing earlier than baryonic matter created a fertile environment for the rich structure that followed: superclusters, clusters, groups, and galaxies. Galaxies are formed in haloes of dark matter(29)(30). These diffuse haloes gravitationally began the formation of galaxies through the formation of clusters of stars(31), before the clumps of stars formed the galaxies we observe today.

2.4 Galaxies

Galaxies are an integral part of our understanding of the universe. We observe them today as large structures from which stars form. How the intricate structure of a galaxy evolves requires a dissection of the classification of galaxies and their component parts.

The first observations that showed evidence for a grander structure in the universe came in 1924(32) when Edwin Hubble used observations of Cepheid variable stars in the Andromeda galaxy to determine their distances from earth. These observations showed that these stars could not be members of the Milky Way galaxy, and Hubble posited that the “nebulae” the Cepheids resided in were separate galaxies. This observation of external galaxies led to the morphological classification scheme of galaxies(33). This classification is known as the “Hubble Tuning-fork” or “Hubble Sequence.”

Galaxies can be separated into several natural entities. There is non-baryonic matter, which is distributed in a diffuse halo. Dark matter does not emit light, and little is known about the distribution of the diffuse halo. The baryonic matter components of a galaxy are stars, gas, and dust. The area between the stars is known as the

interstellar medium, which hosts interstellar gas and dust.

The observational signature of stars is the starlight produced by fusion reactions occurring internally. Observational signatures of dust are in the effects of extinction of light, discussed earlier in section 2.2. Observational signatures of gas can be inferred from absorption features of starlight produced by an intervening cloud of interstellar gas. As the cloud absorbs some of the star's light, absorption lines in the star's spectrum can give an understanding to the chemical composition of the gas.

Stars are born in clouds of molecular gas. This gas is quite dense ($n \approx 300 [cm^{-3}]$) compared to other interstellar material. It also is quite cool, with average temperature of $T \approx 10 - 30 K$. Lower temperatures allow for less radiative pressure halting collapse of molecular clouds to form stars. This cold temperature also hinders emission spectra from the most abundant molecule within these clouds, H_2 . A useful tool to probe these clouds is thankfully the next most abundant element, CO . Carbon-monoxide produces emission lines in the radio frequency, which is more readily emitted at low temperatures. This allows for mapping of molecular clouds from CO observations. CO is a central tracer for molecular gas and the H_2 content within these clouds.

In terms of chemical composition, the interstellar medium is mostly hydrogen ($\sim 90\%$ number density fraction) with slight contributions of helium ($\sim 10\%$ number density fraction) and a smattering of heavier elements ($\lesssim 1\%$ number density fraction) such as C, N, and O. The H and He abundances are derived mainly from the aftermath of the big bang. H and He are depleted into heavier elements as stellar populations progress through their natural life cycle. This gives rise to the measure of metallicity, which measures the relative abundances of heavy elements in comparison to hydrogen.

$\sim 90\%$ of the baryons in the universe are located within the inter-galactic medium, the hot gas between galaxies. The remainder of the baryons are located in galaxies.

Of the remaining baryons, $\sim 80\%$ of the mass is in stars, $\sim 10\%$ of the mass is in molecular clouds, and $\sim 10\%$ of the mass is in atomic gas(34). A useful metric for measuring gas in galaxies is the gas fraction f_{frac} , which relates the proportion of a galaxy's gas mass in relation to its stellar mass content $\frac{f_{gas}}{f_{star}}$.

2.4.1 Classifications of Galaxies

The Hubble sequence of classifying galaxies was created in the early 20th century and many revelations about galaxy evolution and dynamics have occurred since that time. Slight modifications to the sequence have occurred in the scientific community over the past century. Today, a commonly used metric in galaxy classification is the Sérsic index n . The Sérsic index is used to create the Sérsic profile, which describes how the intensity of light varies a distance R from the center of the galaxy. The equation for the general Sérsic profile is

$$I(R) = I_e \exp \left(-b_n \left[\left(\frac{R}{R_e} \right)^{1/n} - 1 \right] \right) \quad (2.14)$$

where R_e is the radius of the galaxy encompassing half of the light emitted, I_e is the intensity at the half-radius, and $b_n = 2n - \frac{1}{3}$ is a constant(35). Most galaxies have a Sérsic index of $\frac{1}{2} < n < 10$.

Irregular Galaxies

There also are galaxies with weak or no regular structure. Hubble described these galaxies as irregular galaxies. Irregulars are not a common type of galaxy, and it should not be used as a modern classification scheme. Observations have shown that many irregular galaxies can be the result of galaxy interactions. Interactions are

discussed in section 2.4.2 in detail.

Elliptical Galaxies

Elliptical galaxies are smooth and symmetric, with an elliptical mass of stars surrounding the central core of the galaxy in a disk arrangement. Elliptical galaxies are generally redder than their counterparts due to the older age of their member stars, and thus star formation in ellipticals is rare.

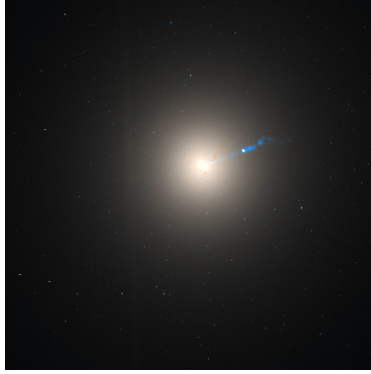


Figure 2.11 M87(36)



Figure 2.12 M89(37)

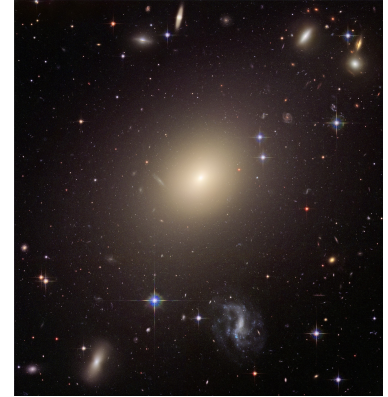


Figure 2.13 ESO 325-G004(38)

Elliptical galaxies are further classified on a scale from 0-7 by their ellipticity. E0 galaxies are circular while E7 galaxies appear elongated like a medication capsule. Elliptical galaxies are found closer to the center of galaxy clusters(39), and are not the dominant type of galaxy within the universe today.

The light intensity of elliptical galaxies can be modeled classically using a De Vaucoulers' profile(40)

$$I(R) = I_e e^{-7.669[(\frac{R}{R_e})^{\frac{1}{4}} - 1]} \quad (2.15)$$

where I_e corresponds to the intensity at a distance R from the center. De Vaucoulers's profile is actually a Sérsic profile with $n=4$. Elliptical galaxies are not limited to the

De Vaucoulers profile, and in reality exhibit Sérsic profiles with a range of Sérsic indices. Despite smooth luminosity profiles, deviations occur at very faint levels. These anomalies are due to cold gas and associated dust(41).

The central component of elliptical galaxies can be modeled by a central stellar mass surface density profile, which describes the intensity of light in the central component. Physically speaking, the centers of ellipticals are classified as containing a core, a cusp, or lack of a core(42). The presence and strength of a core corresponds to a more luminous galaxy with slower rotation and a higher Sérsic index(43). A common way to classify elliptical galaxies is the Faber-Jackson relation(44). This power law relationship describes the luminosity L and the central velocity dispersion of an elliptical galaxy σ with a power index $\gamma = 4$.

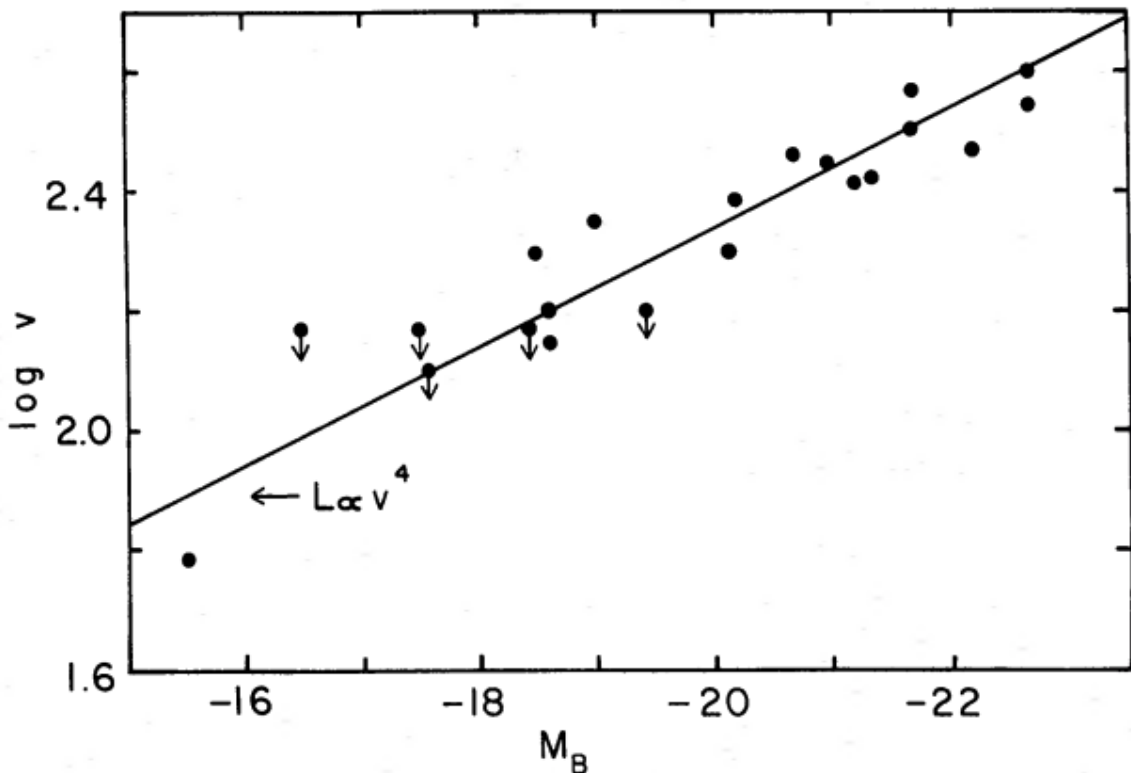


Figure 2.14 The Faber-Jackson relation describing the luminosity of elliptical galaxies versus the central stellar velocity dispersion(44)

The "disk" or fundamental plane of elliptical galaxies have interesting kinematics that are still not fully understood due to disagreements between observation and theory. Observations show a relationship between half light radius r_{50} , half-light surface brightness I_{50} and velocity dispersion σ . Observational results show the relationship $r_{50} \propto \sigma^\alpha I_{50}^\beta$ has best fit parameters $\alpha = 1.3$ and $\beta = -0.76(45)$, while theory suggests parameters $\alpha = 2$ and $\beta = -1(46)$. The favored explanation for deviation from theory is a variation in the stellar mass to dynamical mass ratio. In general, massive systems are slower rotators that are closer to perfect ellipsoids while lower mass systems are faster rotators that have a stronger tendency to be disk(47).

Some elliptical galaxies show evidence for recent star formation, particularly in lower mass systems(48). However, Balmer absorption features in elliptical galaxies trace a strong link to older stellar populations. K giant stars are the dominant member, however they are spanned by a mixture of stellar types depending on the age and metallicity of the population(49).

As the bias to older stellar populations would indicate, elliptical galaxies contain a small amount of cold atomic and molecular interstellar gas(50). It is not a dominant baryonic component, comprising $\leq 1\%$ of the total mass of the elliptical system(51). HI gas is distributed in elliptical galaxies in either a ring around the center of the system, or in an irregular tail or cloud offset from the center of the galaxy(52). The HI content is uncorrelated with the age and stellar kinematics of the disk. H_2 content in ellipticals is distributed in a disk with higher angular momentum than the stellar component. In certain cases, the molecular gas component is counter-rotating with respect to the stellar component. This could suggest an external origin of the molecular gas component(53), as arguments for stellar recycling anticipate ~ 10 times the amount of observed molecular gas. Where recycled gas goes is still an unsolved problem, and the full nature of gas in elliptical galaxies is still relatively

misunderstood.

Lenticular Galaxies

Lenticular galaxies are classified in the Hubble tuning fork between spiral galaxies and elliptical galaxies. They are disk galaxies with a smooth star dispersion and low star formation rates(54). The low star formation rates are physically explained by dust retention within their disks(55).

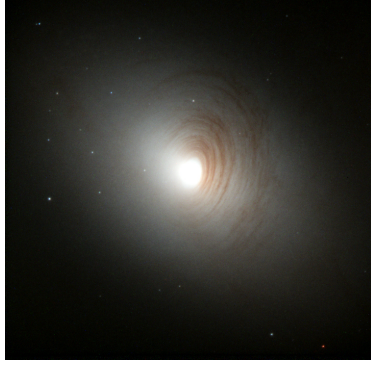


Figure 2.15 NGC 2787
(NASA Hubble)



Figure 2.16 NGC 6861
(NASA Hubble)

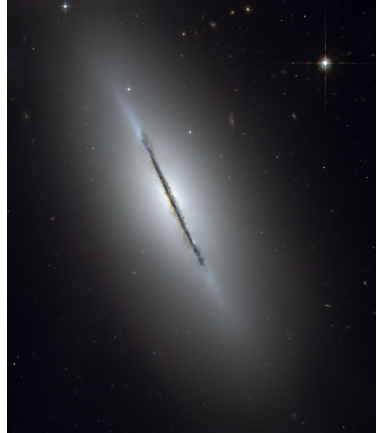


Figure 2.17 NGC 5866
(NASA Hubble)

A defining characteristic that differentiates lenticular galaxies from spiral galaxies is a lower molecular gas mass content, resulting in a lack of spiral structure. The shorthand for lenticular galaxies within the Hubble scheme is S0.

Despite tremendous physical difference, lenticular galaxies are photometrically quite similar to elliptical galaxies. The central question surrounding lenticular galaxies is if they are spirals that ran out of gas before becoming redder, or something else. The prevailing hypothesis for the formation of lenticular galaxies is that they are the product of merging systems. Observational studies have shown that lenticular galaxies become relatively more frequent as you approach the center of clusters, but

the subjectivity in classification methods available provides issues when making such sweeping conclusions.

Spiral Galaxies

Spiral galaxies are the most common type of galaxy in the universe. They are disk galaxies with active star formation. They have two distinct components, a central bulge and a disk. They exhibit arms that spiral from the center of the galaxy along the plane of the disk. The center of the galaxy contains a smooth red component called a bulge. The bulge of a galaxy can be further classified by type as being a classical bulge, a pseudobulge, or a bar. In spiral galaxies, the Sérsic index n represents the balance between the bulge and the disk, as they are distinct and separate components.



Figure 2.18 Pinwheel Galaxy (NASA/ESA)



Figure 2.19 NGC 5055 (NASA/ESA)

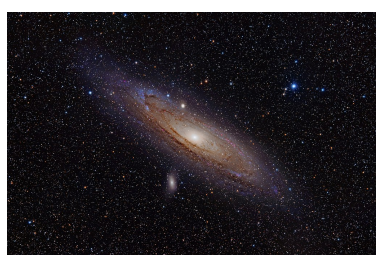


Figure 2.20 Andromeda Galaxy (NASA/ESA)

The gas and stars in spiral disks are rotationally supported objects. As a result, there is a strong relationship between the mass and rotational velocity of spiral galaxies(56). The mass is calculated from the intrinsic luminosity of the galaxy, while the rotational velocity can be determined from the spectral line width of the galaxy. This relation has also been determined for the overall baryonic component of spiral galaxies(57).

Classical bulges in the center of spirals commonly (but not exclusively) contain older

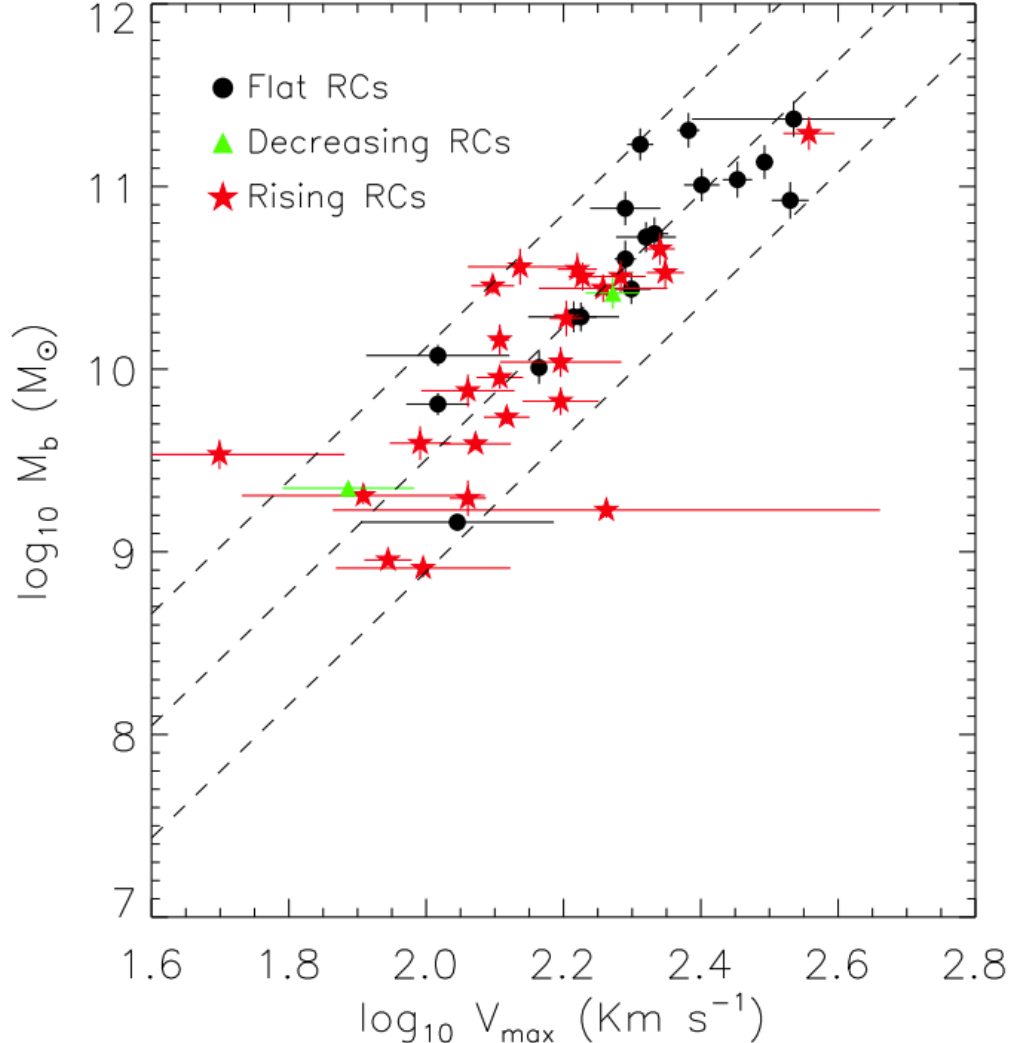


Figure 2.21 The Tully-Fisher relation for spiral galaxies using results from the GHASP sample, which follows $M_{bar} = 10^{2.21 \pm 0.61} V_{max}^{3.64 \pm 0.28}$ (57)

stellar populations in comparison to the spiral arms in the disk surrounding the bulge(58). Classical bulges usually (but not exclusively) have a Sérsic index of $n > 2$ (59). Pseudobulges are flatter than classical bulges with star formation surrounding the nucleus of the galaxy(60). Pseudobulges have a Sérsic index of $n < 2$ (61). Differentiation between pseudobulges and bulges can be inferred from integral field spectroscopy(62). Bars are elongated stellar structures within the central regions of disk galaxies, which are an entirely separate stellar population from the disk of the galaxy(60)(63). In galaxies with edge-on orientations, bars produce a boxy or peanut-

shaped bulge(64). Bars exhibit higher rates of star formation both in and around the nucleus of the galaxy(65). Current observations of the Milky Way indicate it is a spiral galaxy with a bar.

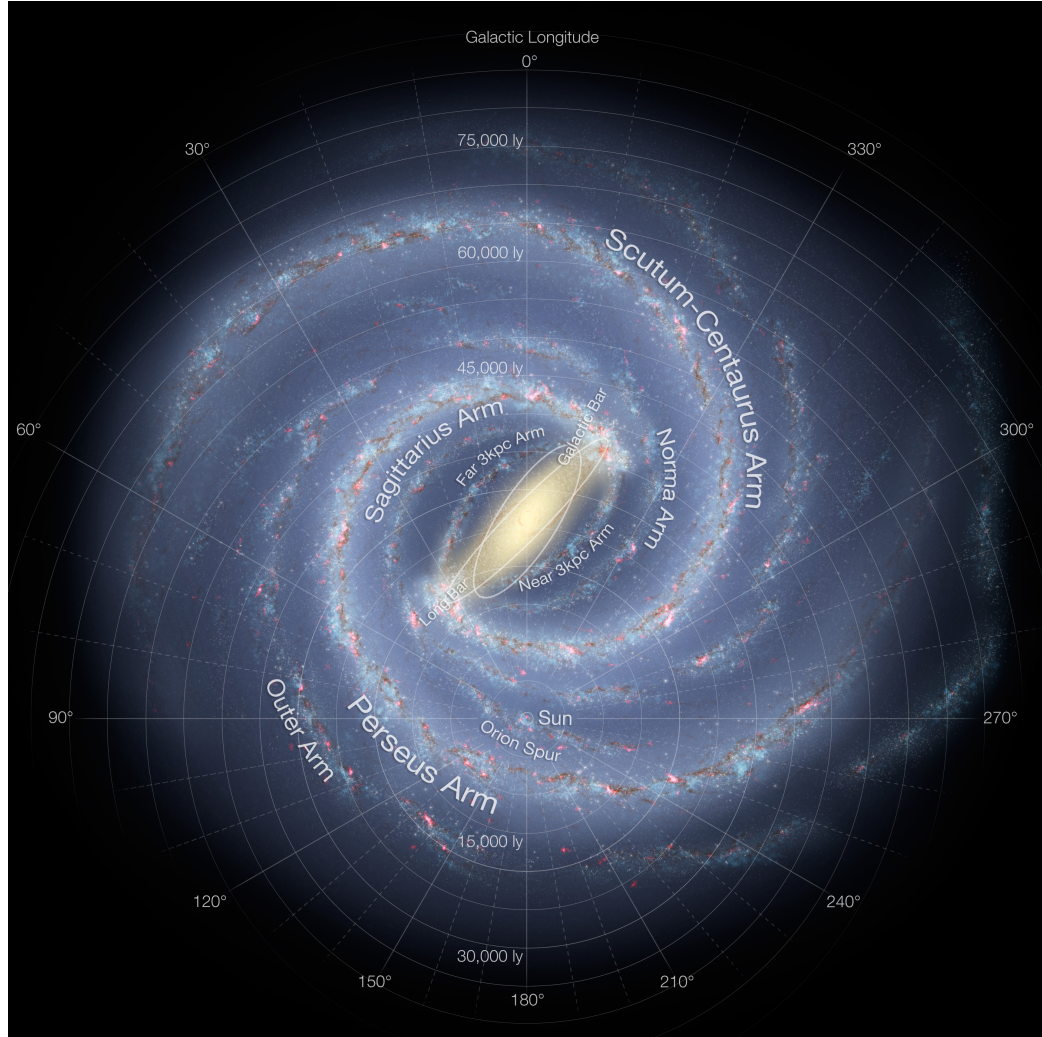


Figure 2.22 A map of our home galaxy, the Milky Way(66). The central bar and different spiral arms are the defining features of the spiral structure of the Milky Way.

Spiral galaxies host gas within their spiral disk, with a high concentration of cold gas inside them. Luminous spiral galaxies contain $\sim 10 - 20\%$ of their baryonic content in the form of neutral hydrogen and molecular clouds. Atomic hydrogen can be traced through the 21-cm hyperfine transition, while molecular hydrogen can

be traced through the next most abundant element with higher rates of emission: CO($1 \rightarrow 0$). Lower mass spirals have a higher atomic mass content than more massive galaxies, which have depleted the gas content at a more efficient rate(67).

The dust mass is a minuscule portion ($\sim 0.1\%$) of the baryonic mass budget in spiral galaxies(9). The importance of dust on the evolution of galaxies and our observations of them is not related to a galaxy's overall mass. Efficient absorption of UV and optical light by dust grains is re-radiated in the infrared spectrum(68). As a result, UV and optical light only traces unobscured star formation while infrared light traces the rest. The effects of extinction are amplified for spiral galaxies at inclinations where the line of sight is along the disk of the galaxy(69). Similar to molecular gas content, the dust-to-gas ratio is strongly correlated to galaxy mass. This is shown through a dependence between inclination-dependent reddening and the overall mass of systems(70).

2.4.2 Galactic Interactions

Observing galaxies on the limited timescale available to astronomers could lead to the elementary inference that galaxies are not dynamic systems. However, galaxies can merge to form new galaxies. Interactions between galaxies is a key part of galaxy evolution. One of the main observational techniques for locating merging galaxies is searching for signatures within images and counting close pairs of galaxies. This technique relies on human interpretation and is somewhat biased as a result.

A more objective approach involves searching for asymmetry caused from mergers. This technique is slightly skewed based on the assumption that any asymmetry caused from perturbations during a merger is visibly detectable. A comparison of the two techniques may indicate that samples of close pairs of galaxies are a sample of the

pre-merger population, while samples of perturbed galaxies give a snapshot of merged galaxies at a later stage of the merging process(71).



Figure 2.23
NGC 2623 (NASA Hubble)



Figure 2.24
Antennae Galaxies (NASA Hubble)



Figure 2.25
Mice Galaxies (NASA Hubble)

Galaxy mergers can form resulting starburst galaxies exceptionally high rates of star formation. Close pair mergers show an increase of $\sim 1.5 - 2$ in the star formation rates relative to a control field sample(72). While close pair galactic mergers are rarely associated with true starbursts, they account for $\sim 40\%$ of the starburst galaxies in the universe. The gas driven towards the center of a gas-rich merging system is the primary process producing the high abundance of starburst galaxies(73).

The luminosity of infrared galaxies is driven by dust obscured star formation. As a result, the most luminous infrared galaxies are often associated with major mergers(74). The star formation rates in any galaxy is directly related to the gas content of the galaxy. Merging systems that are gas-rich are called "wet" mergers. Mergers between galaxies with low gas content are called "dry" mergers. Dry mergers do not have a connection to higher rates of star formation in the merged galaxy due to their low gas content.

Post-starburst galaxies are another subgroup of galaxies associated with mergers. They are characterized by a lack of ionized gas. This is indicated from a lack of

high energy stars (O & B type), which exhibit a spectrum lacking $H\alpha$ and other emission lines. Post-starburst spectra exhibit Balmer absorption lines, indicating A-type stars(75). Due to the lifetime of A stars, the galaxy must have concluded star formation within $\sim 10^9$ years of the merger. Post-starburst galaxies are a rare but frequently studied subset of galaxies, and it is unclear if mergers are the only formation mechanism. Another possibility is a ram pressure stripping event where the motion of gas from a nearby galaxy moves through another galaxy, stripping and perturbing the gas content to induce another star formation epoch within the galaxy. The exact formation mechanism(s) of post-starburst galaxies are still relatively undetermined.

Discussion has centered on the luminous objects within a galaxy, mainly stars. Stars are baryonic, and the main luminous source within this study. However, black holes are a non-luminous object that could be considered baryonic. Bulges are defined by a central super-massive black hole in the center of the spheroid of stars. The mass of the central black hole is closely related to the velocity dispersion of the host galaxy(76). This evidence points to a close relationship between spheroid formation and the growth of super-massive black holes(77). The mass of the central black hole in a galaxy is thus closely related to the the mass of the central bulge, which is primarily stars. The total mass of the central black hole in comparison to the total baryonic matter content of the galaxy is also small. The correlation between the central bulge mass with black hole mass, in addition to negligible impact on the total baryonic matter content of the galaxy were the driving factors for the exclusion of black holes from this study.

Chapter 3

Calibrating Dust and Cold Gas Content

The goal of this study is to provide a precise calibration of the dust and cold gas content of star-forming galaxies. An indirect measure of the effects of these constituents lies in the Balmer decrement. In galaxies with higher dust and gas content, higher Balmer decrements are expected as $H\beta$ is extinguished less than $H\alpha$. If galaxies have measures of cold-gas and dust mass independent of the Balmer decrement, a correlation between the Balmer decrement and the mass component should also exist. Using this physical relationship, the following formula for each mass component M_\diamond can be derived.

$$M_\diamond = m \times \log \left(\frac{H\alpha}{H\beta} \right) + b \quad (3.1)$$

In this study, a linear Markov Chain Monte-Carlo method was applied to reduced xCOLD GASS(78) and JINGLE(79) surveys to determine m and b for each mass component M_\diamond . Stellar masses from SDSS DR-7 were used in concordance with results obtained from the MCMC constraints to apply these results to a wider sample

of galaxies.

3.1 MCMC Methods

Markov chain Monte-Carlo (MCMC) methods are used to approximate the parameters m and b within the best-fit equation 3.1. MCMC constructs chains that explore parameter space to find the best-fit parameters of m and b that minimize the offset from the model with the sample data. The parameters are selected by constructing an approximation of the posterior probability distribution of the sample function.

The posterior probability distribution of a sample represents the range of values of the sample and the probability of observing each value. This distribution is composed of two distributions: the likelihood and prior distributions.

$$\text{Posterior Probability} \propto \text{Likelihood} \times \text{Prior Probability} \quad (3.2)$$

The likelihood distribution describes how the sample itself is distributed, while the prior represents the pre-conceived beliefs on the data. In the context of this survey, the prior distribution is relatively straightforward. I define ranges of parameters based on functional relationships between the Balmer decrement and the mass element in table 4.1. If the parameter lies outside of the prior range, the prior probability is set to 0. Equation 3.2 dictates that if the prior probability is 0, the posterior probability is 0. This means that if a parameter value is drawn outside of the pre-defined range, that value is not allowed for further selection within the chain. If the parameter lies within the prior range, the prior is set to 1 and the likelihood is the only factor determining the posterior distribution. This prevents erroneous contributions to the posterior distribution, requiring the posterior to be related only to the likelihood

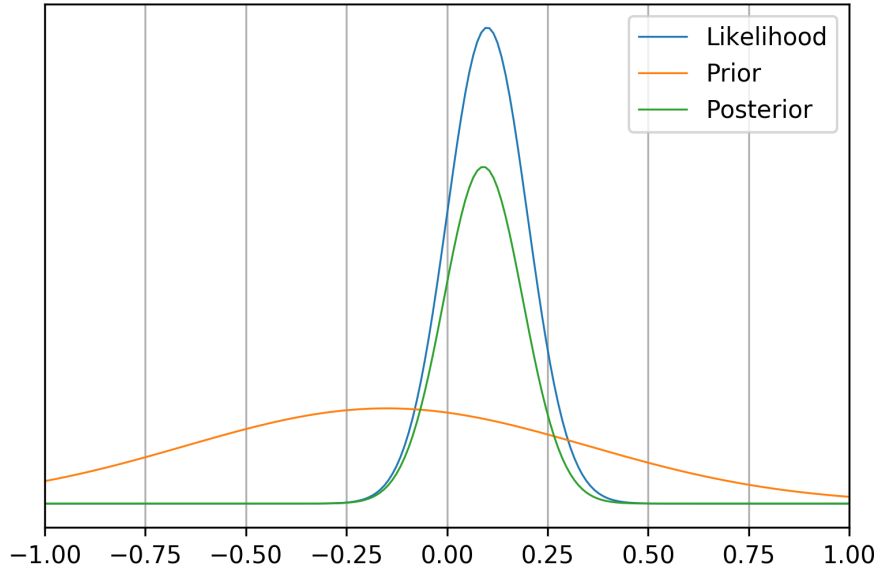


Figure 3.1 A plot detailing how the prior ($N(\mu = -0.15, \sigma = 0.5)$) and likelihood ($N(\mu = 0.1, \sigma = 0.1)$) probability distributions affect the posterior distribution

function when the parameter is within the pre-defined range.

To construct a chain, an initial guess based on the sample data was made for all parameters. The chain is allowed to progress by creating clusters of points around the starting guess and selecting values of the parameter that closest resembles the probability distribution of the sample data. The algorithm that performs this is the stretch-move algorithm, which is noted for its efficiency. Simply, the algorithm selects the next parameters in the chain based on the probability distribution of the previous parameters in the chain(80).

For a linear model, log-likelihood distribution is given by

$$p(y_n, x_n | m, b, S_n) \propto \frac{1}{\sqrt{2\pi\Sigma_n^2}} \exp\left(-\frac{\Delta_n^2}{2\Sigma_n^2}\right) \quad (3.3)$$

where $p(y_n, x_n | m, b, S_n)$ describes the probability of observing the data y_n and x_n given the straight line parameters m , b , and the uncertainty tensor $S_n = \begin{pmatrix} \sigma_{x,n}^2 & 0 \\ 0 & \sigma_{y,n}^2 \end{pmatrix}$ of the n th data point. Δ_n is the deviation from the n th data point, described as $\Delta_n = y_n - mx_n - b$. $\Sigma_n^2 = \vec{v}^T (S_n + \Lambda) \vec{v}$ with $\vec{v}^T = (-m, 1)$, and Λ represents the intrinsic scatter of the model. In this survey, the scatter was interpreted as perpendicular to the model-line with some variance λ and is written as $\Lambda = \frac{\lambda^2}{1+m^2} \begin{pmatrix} m^2 & -m \\ -m & 1 \end{pmatrix}$. This form, derived by (81) describes the likelihood function used by the stretch-move algorithm to select the next parameters within the chain. These chains are detailed in figures 4.4, 4.8, and 4.12.

These parameters or "walkers" walk through parameter space before converging upon parameter values that represent the best-fit of the sample data. To account for the random walk from the initial guess, the first portion of the chain is discarded. This is called the burn-in period, which was set to 5×10^4 steps within this study. After the burn-in period the chain was allowed to explore parameter space for 10^6 steps, which allowed for sufficient mixing of the chain. Each step along the chain contributes to the density of each parameter, and the values of the parameter density are distributed normally surrounding the best fit value. The best fit value was taken as the median value of the density distribution of the chain. The uncertainty in each parameter was selected as the 1σ deviation from the median value. The density distributions are detailed in figures 4.5, 4.9, and 4.13.

A full explanation of MCMC methods is beyond the scope of this document. For further reading and discussion of MCMC methods, please see (80) and (82).

3.2 Gas mass calibrations

H_2 is the most abundant molecule within the interstellar medium (ISM). Despite tremendous abundance, it does not experience high rates of radiative transition due to the cold environments H_2 usually occupies. The next most abundant molecule CO , emits in the radio wavelength regime. CO emission at 2.6mm is easily detected using modern microwave telescopes. CO can thus be used as a tracer of the cloud of molecular gas in its surroundings(83).

$$M_{H_2} = \alpha_{CO} L_{CO} \quad (3.4)$$

To convert from $CO_{1\rightarrow0}$ emission to molecular gas mass, a conversion factor α_{CO} is used. The central observation used in accurately calibrating α_{CO} is [C II] emission ($158\mu m$). [C II] is a tracer of dark molecular gas, and an important coolant of the interstellar medium. [C II] is prevalent in molecular photo-dissociation regions of ionizing radiation, as well as the ionised and atomic phases of the ISM. [C II] and $CO_{1\rightarrow0}$ emission can trace the molecular content over grand scales, as well as slight variations in α_{CO} .

External factors used to consider deviations in calibrations of α_{CO} are galactic metallicity and deviation from the galaxy star-formation plane(85).

$CO_{1\rightarrow0}$ emission relies on dust content to shield it from ionizing radiation which can photo-dissociate CO into C^+ and O . Therefore, galaxy environments with higher dust-to-gas mass ratios exhibit lower rates of photo-dissociation. As a result, galaxies with higher metallicities exhibit lower CO flux and underestimate α_{CO} .

In addition to the effects of metallicity on the strength of $CO_{1\rightarrow0}$ flux, the strength

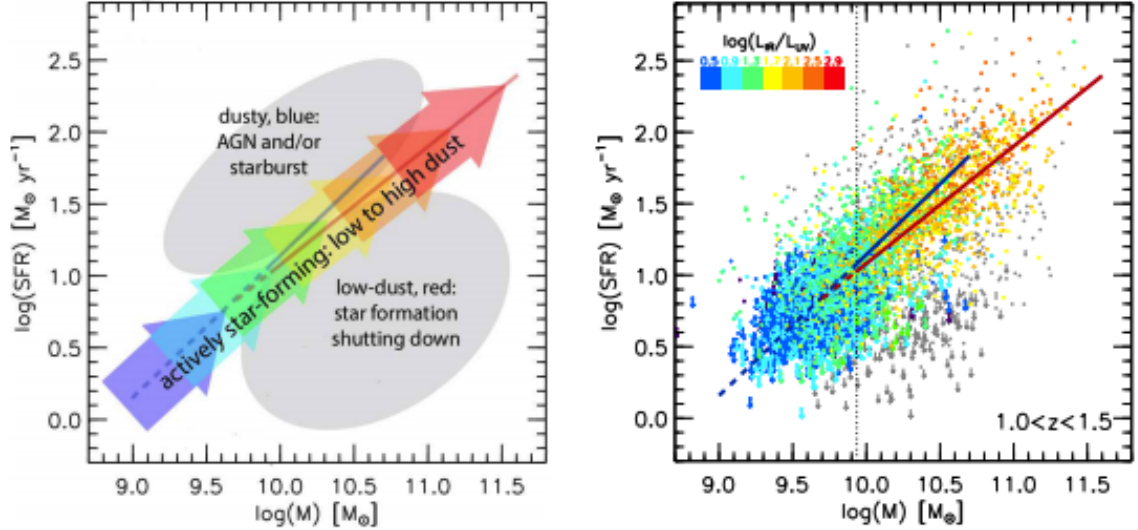


Figure 3.2 Figure from (84) showing the star-formation stellar mass plane. Galaxies that are actively forming stars are classified as main sequence star-forming galaxies. As galaxies exhaust their star-forming resources, the star-formation rate of the galaxy decreases. Galaxies in this later evolutionary stage of evolution are in the lower group of galaxies.

$$\log \alpha_{CO}(\pm 1.462) = 15.623 - 1.732[12 + \log(O/H)] + 0.051 \log \Delta(MS)$$

Figure 3.3 Calibrated α_{CO} conversion function with independent calibration from molecular gas depletion timescale(85)

of the ionizing radiation field that causes photo-dissociation can be measured from the deviation from the star formation plane. Galaxies with higher star formation rates have stronger radiation fields. Stronger radiation fields result in higher rates of photo-dissociation of CO . When comparing the star-formation rates of an observed galaxy to galaxies with similar stellar mass and redshift, the effects of the radiation field strength can be accounted for.

The star formation rate of a main sequence galaxy with mass M_* and redshift z is defined (84) as

$$\log(sSFR_{ms}(z, M_*)) = -1.12 + 1.14z - 0.19z^2 - (0.3 + 0.13z)(\log M_* - 10.5)[\text{Gyr}^{-1}] \quad (3.5)$$

The offset from the main sequence is thus defined by (85) as

$$\Delta(MS) = \frac{sSFR_{measured}}{sSFR_{ms}(z, M^*)} \quad (3.6)$$

The deviation from the star-formation main sequence and the metallicity of a galaxy must be accounted for in order for a precise α_{CO} , and M_{H_2} from the conversion.

3.3 Dust mass calibrations

Data for the dust mass of galaxies was obtained from the JINGLE survey sample(79).

The sample applies photometric results from a variety of wavelength passbands: $22\mu m$ (WISE), $60\mu m$ (IRAS), $100\mu m$, $160\mu m$ (Herschel/PACS), $250\mu m$, $350\mu m$, $500\mu m$ (Herschel/SPIRE), and $850\mu m$ (SCUBA-2)(86). Using a wide range of passbands, it is possible to construct a spectral energy distribution (SED) of the galaxies within the sample. This relationship shows how the strength of incident radiation changes as a function of wavelength of light, from $2 - 850\mu m$.

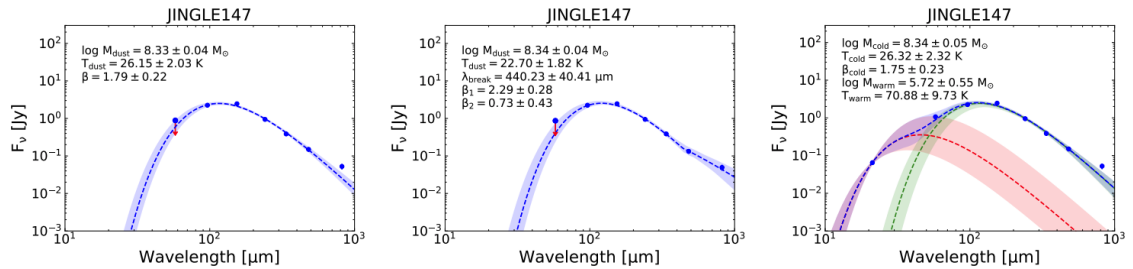


Figure 3.4 Examples of an SED of one galaxy in the JINGLE sample(79), fitted with the single-modified black body (SMBB, left), the broken emissivity law modified black-body (BMBB, middle), and the two modified black-bodies (TMBB, right) models.

The SED's of galaxies were fitted using separate models of dust populations according

to the SED characteristics. The models differ due to assumptions regarding the types of dust populations within the galaxy(87). The fitting methods used were Bayesian, and the free parameters used for each galaxy varied based on the model type. Using these fitting methods, the dust mass of galaxies can be derived.

	SMBB	BMBB	TMBB
F_λ	$F_\lambda = \frac{M_{Dust}}{D^2} \kappa_\lambda B_\lambda(\lambda, T)$	$F_\lambda = \frac{M_{Dust}}{D^2} \kappa_\lambda B_\lambda(\lambda, T)$	$F_\lambda = F_\lambda^{SMBB_{cold}} + F_\lambda^{SMBB_{warm}}$
κ_λ	$\kappa_\lambda = \kappa_0 \left(\frac{\lambda_0}{\lambda}\right)^\beta$	$\kappa_\lambda = \begin{cases} \kappa_0 \left(\frac{\lambda_0}{\lambda}\right)^{\beta_1} & \text{if } \lambda < \lambda_b \\ \kappa_0 \left(\frac{\lambda_0}{\lambda_b}\right)^{\beta_1} \left(\frac{\lambda_b}{\lambda}\right)^{\beta_2} & \text{if } \lambda > \lambda_b \end{cases}$	κ_{warm} and κ_{cold} using $\kappa_\lambda = \kappa_0 \left(\frac{\lambda_0}{\lambda}\right)^\beta$
N_{free}	M_{Dust}, T, β	$M_{Dust}, T, \beta_1, \beta_2, \lambda_b$	$M_{cold}, T_{cold}, \beta_{cold}, M_{warm}, T_{warm}$

Table 3.1 The three different models(87) used to describe the dust masses as a product of the SED of the host galaxy. D denotes the distance to the galaxy, B_λ denotes the Boltzmann distribution at a temperature T (equation 2.1), κ_λ denotes the dust mass absorption coefficient. κ_λ varies based on the model used, and depends on the dust emissivity index β to describe which dust mass gives rise to an observed luminosity. In the TMBB, β_{warm} was assumed equal to 1.5(88) to minimize the number of free parameters.

3.4 SDSS

Stellar masses for galaxies within this survey come from the Sloan Digital Sky-Survey (SDSS) DR-7 release of measurements(89). SDSS uses fiber optic cables mounted to an aluminum plate in order to obtain spectral data, allowing for multiple spectra to be obtained simultaneously. The imaging camera was mounted to a 2.5m telescope at Apache Point Observatory, New Mexico. The camera houses 5 rows of 6 CCD's (figure 2.3), with each row according to a different filter.

Stellar masses are derived from SDSS photometry using the u , g , r , i , and z filters of SDSS(90). The magnitudes obtained in each filter are corrected for emission lines by assuming that the contribution of emission lines obtained by the optical fibre is

the same as the broad band magnitudes obtained by the CCD. The effect of emission lines on broad band magnitudes is usually <0.1 mag but is unlikely to be completely correct.

Mass estimates using photometry are more constrained at lower ($M < 10^{10}M_{\odot}$) total stellar masses than using the fiber and spectral features only. Most of the galaxies used within this survey have stellar masses that fall within this range, and thus the method involving photometry and spectral adjustments is selected for this survey.

Chapter 4

Results

4.1 Sample selection

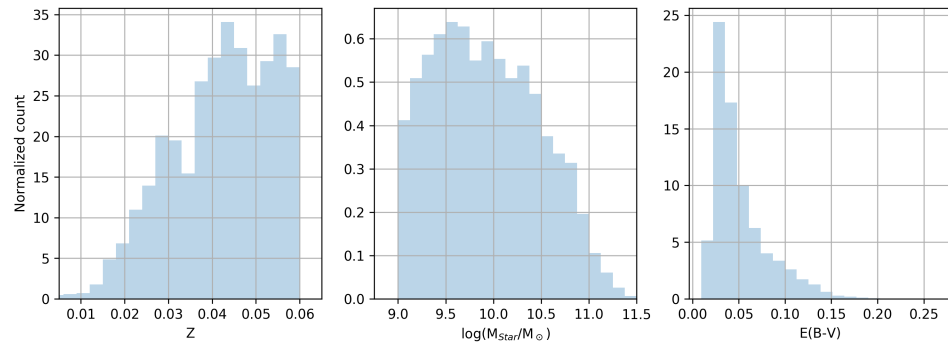


Figure 4.1 Histograms detailing the distribution of SDSS galaxy sample after data reduction. Histograms show galaxy redshift (Z), stellar mass ($\log\left(\frac{M}{M_{\odot}}\right)$), and $E(B-V)$ color

In order to apply the results from MCMC constraints, consistency of galaxy properties across different galaxy surveys is required. To improve spectroscopic signal input, a signal-noise threshold of 5 was placed on all galaxies. This improved spectroscopic data quality to provide a more precise calibration. In addition to signal constraints,

the sample of galaxies was limited to star-forming galaxies.

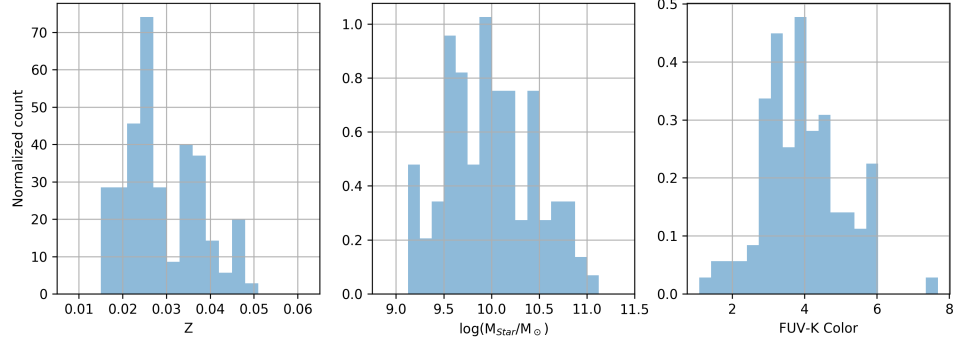


Figure 4.2 Histograms detailing the distribution of JINGLE galaxy samples used for MCMC calibration. Histograms detail galaxy redshift (Z), stellar mass ($\log \left(\frac{M}{M_{\odot}} \right)$), and FUV-K color

Passive galaxies exhibit weak Balmer emission lines, while active galactic nuclei have an emission excess in all wavelengths. This can have an unmanageable effect on the Balmer decrement. Star-forming galaxies exhibit strong emission lines that are affected by the galactic environment and not the emission characteristics of the galaxy core. The emission classification of star-forming galaxies is signal-noise above 3 in $H\alpha$, $H\beta$, $N[II]$, and $O[III]$ emission lines with minimal contribution from an AGN(91). This allows for a tighter relationship between galaxy properties in star-forming galaxies.

Specific to the xCOLD GASS dataset, I also require the detection of the $CO_{1 \rightarrow 0}$ emission line. This emission line is central to the calculation of gas mass, and its detection is therefore a necessity to the xCOLD GASS sample.

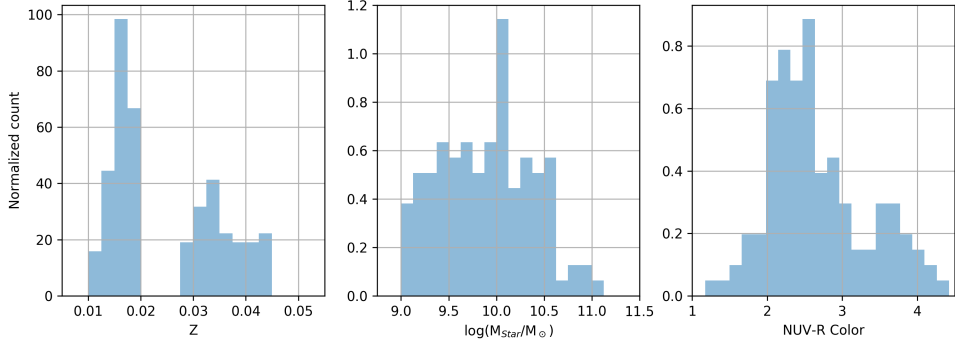


Figure 4.3 Histograms detailing the distribution of xCOLD GASS galaxy samples. Histograms detail galaxy redshift (Z), stellar mass ($\log\left(\frac{M}{M_{\odot}}\right)$), and NUV-R color

4.2 MCMC calibrations

4.2.1 Prior ranges

Component	m_{guess}	m_{low}	m_{high}	b_{guess}	b_{low}	b_{high}	$\ln(f_{guess})$	$\ln(f_{low})$	$\ln(f_{high})$
$\log(L_{CO1 \rightarrow 0})$	10	0	20	3.5	0	7	0	-5	5
$\log(M_{H_2})$	6	0	20	2	0	8	0	-5	5
$\log(M_{Dust})$	4	0	20	5	0	8.5	0	-5	5

Table 4.1 The range of values accessible to the MCMC sampler. The guesses for each parameter were taken from the original sample of data. The ranges accounted for computing time and the functional dependencies and limits of each parameter.

The prior ranges in table 4.1 for use with the MCMC sampler were selected with consideration to physical and computational factors. If parameters were drawn outside of the ranges in table 4.1, the prior probability was set to 0 and the parameter would not be drawn in further steps in the chain. As discussed in sections 2.2 and 3, a positive relationship between the Balmer decrement and any mass component should exist due to the effects of extinction. As a result, m_{low} was set to 0 for all

calibrations. Additionally, upper bounds on the intercept b_{high} were determined by the lower values of M_\odot at the minimum Balmer decrement for each sample. b_{low} was selected as 0 for all M_\odot , as it is physically impossible to have negative mass within these galaxies. m_{high} , $\ln(f_{high})$, and $\ln(f_{low})$ were selected arbitrarily, but accounting for computing time of accessible states available to the sampler, as well as crude estimates of the most extreme values for the slope and scatter of the relation.

The results of the MCMC chains in figures 4.4, 4.8, and 4.12 are summarized in table 4.2. Notably, the scatter of the $\log(L_{CO_{1 \rightarrow 0}})$ calibration was higher than the scatter of the M_{H_2} and M_{Dust} components.

When comparing the calibrator values with the observed values of each component M_\odot , a residual prescription was implemented.

$$M_\odot^{Residual} = M_\odot^{Observed} - M_\odot^{MCMC} \quad (4.1)$$

4.2.2 LCO_{1-0}

The primary use of $\log(L_{CO_{1 \rightarrow 0}})$ is as an observable to determine α_{CO} for accurate conversion to gas mass, M_{H_2} . As noted by (85), the metallicity and deviation from the main sequence also has an impact on α_{CO} . The calibration is well mixed, as evidenced in figure 4.4.

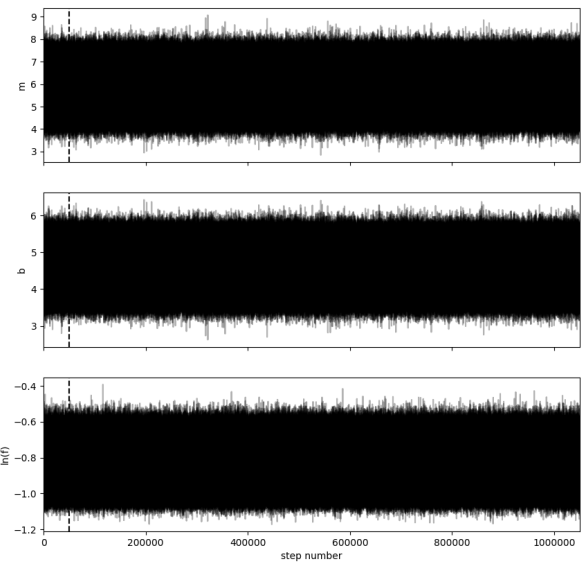


Figure 4.4 The converged Markov chains of the parameters of the Balmer decrement and LCO_{1-0} relation. The dashed vertical line denotes the end of the burn-in period, which was 50,000 steps

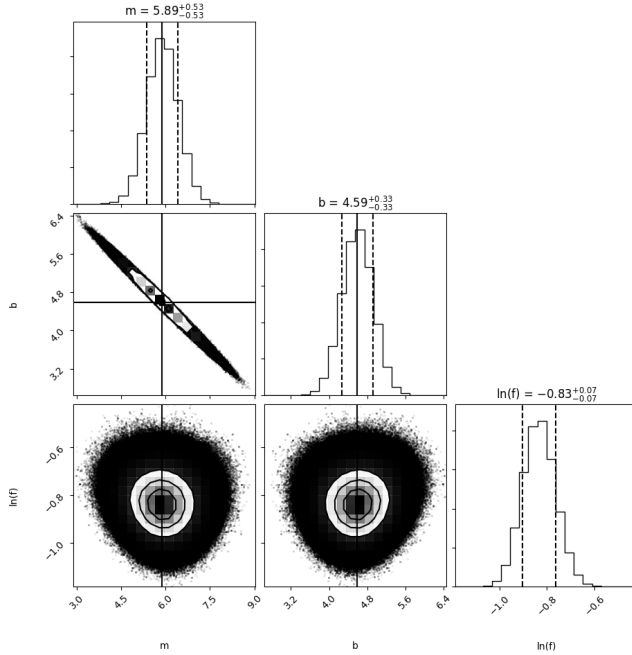


Figure 4.5 The resulting distributions from the chains in figure 4.4, showing the median and $1-\sigma$ (gaussian) standard deviation for each parameter. The MCMC algorithm calculates the scatter in terms of the natural log of the scatter, $\ln(f)$. When converted to log-log scale, the scatter $f = 0.44$

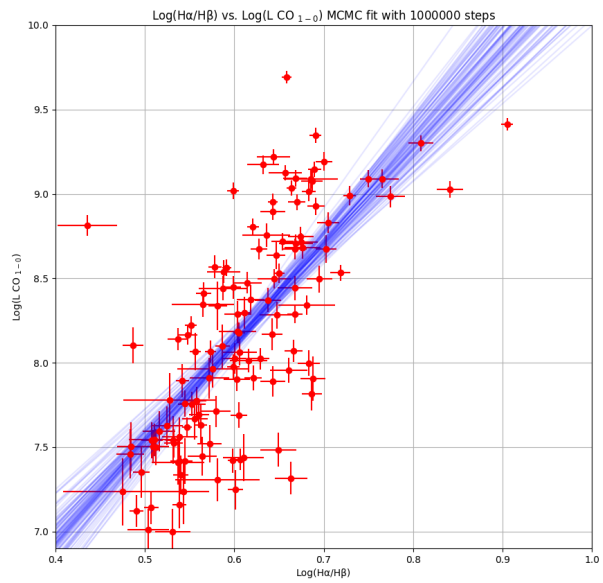


Figure 4.6 $\log(L_{CO_{1 \rightarrow 0}})$ shown on ordinate, $\log\left(\frac{H\alpha}{H\beta}\right)$ shown on the abscissa. 100 random states from the MCMC chain plotted in blue. Measurements of $\log(L_{CO_{1 \rightarrow 0}})$ are shown in red.

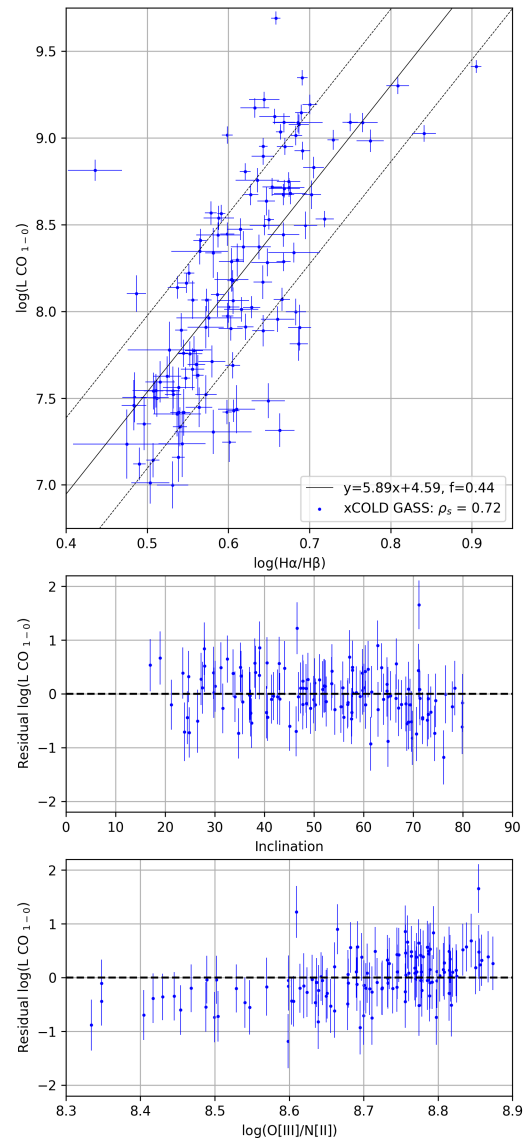


Figure 4.7 Relationships between $\log(L_{CO_{1-0}})$ and the Balmer decrement constrained using median MCMC values the xCOLD sampled set.

Applying the calibrators from figure 4.5 to the xCOLD GASS data set, it allows

examination of other observables with respect to the calibrator. In figure 4.7, the distribution of $\log(L_{CO_{1 \rightarrow 0}})$ and $\log(\frac{H\alpha}{H\beta})$ are imposed with the MCMC calibration. The intrinsic scatter of the calibration is shown with the dashed line above and below the calibrated values.

In comparison of the MCMC calibrated results and the observed $\log(L_{CO_{1 \rightarrow 0}})$ values, inclination and metallicity were selected to search for deviations from the calibration. Examination of the dependencies between inclination and $\log(L_{CO_{1 \rightarrow 0}})$ residual values reveal no distinct trend of overestimation or underestimation of $\log(L_{CO_{1 \rightarrow 0}})$ with respect to inclination. The residual values of $\log(L_{CO_{1 \rightarrow 0}})$ show a distinct trend with metallicity. The calibrator clearly exhibits an overestimation of $\log(L_{CO_{1 \rightarrow 0}})$ at low metallicities, and an underestimation of $\log(L_{CO_{1 \rightarrow 0}})$ at high metallicities. This is displayed in the lower sub-panels of figure 4.7.

4.2.3 Gas Mass

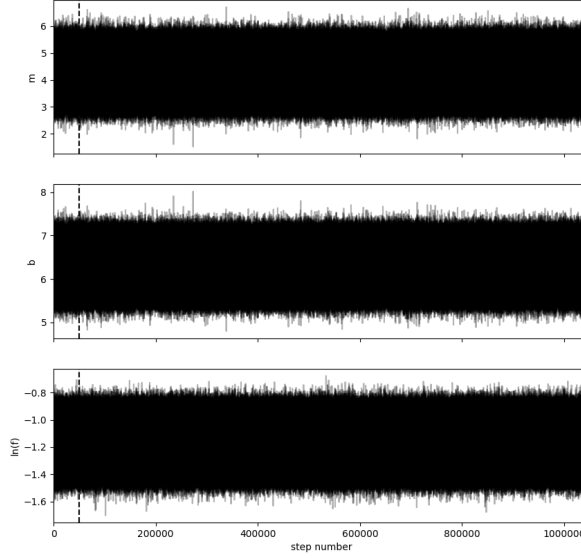


Figure 4.8 The converged Markov chains of the parameters of the Balmer decrement and $\log(M_{H_2})$ relation. The dashed vertical line denotes the end of the burn-in period, which was 50,000 steps

In calibrating $\log(M_{H_2})$, the intrinsic scatter f was lower than the $\log(L_{CO_{1 \rightarrow 0}})$ calibration. Additionally, the values of $1\sigma_m$ and $1\sigma_b$ are much lower for $\log(M_{H_2})$ than $\log(L_{CO_{1 \rightarrow 0}})$ (table 4.2). This was an early indication that $\log(M_{H_2})$ was more tightly correlated to the Balmer decrement than $\log(L_{CO_{1 \rightarrow 0}})$.

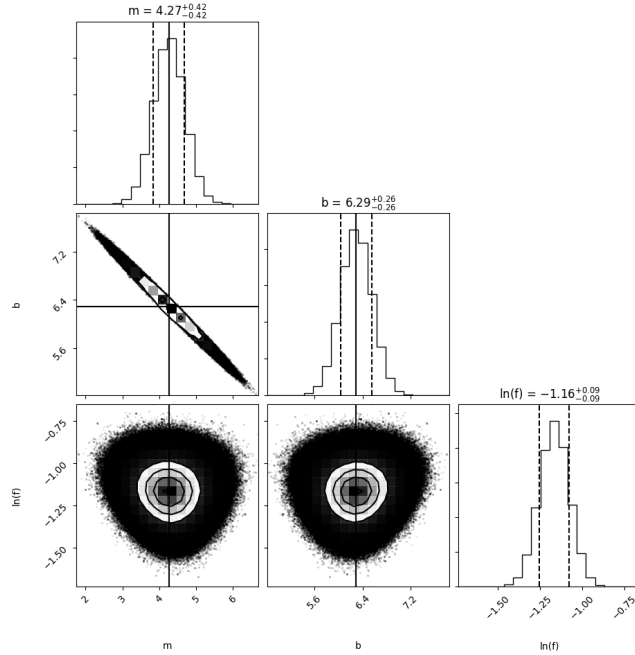


Figure 4.9 The resulting distributions from the chains in figure 4.8, showing the median and $1-\sigma$ (gaussian) standard deviation for each parameter. The MCMC algorithm calculates the scatter in terms of the natural log, $\ln(f)$. When converted to log-log scale, the scatter $f = 0.31$

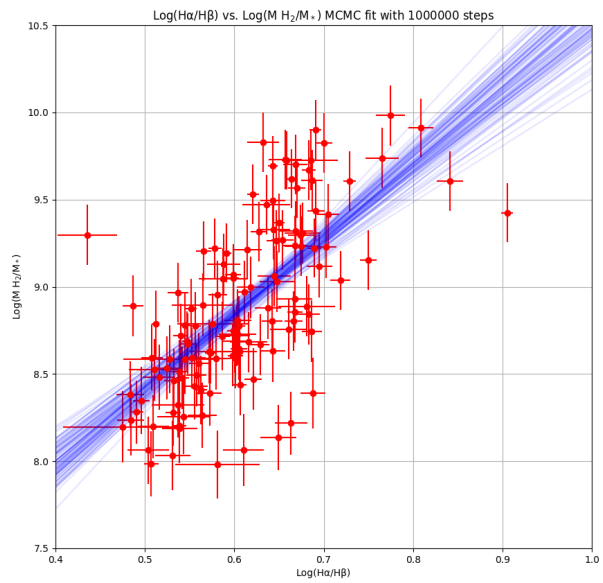


Figure 4.10 $\log(M_{H_2})$ shown on the ordinate, $\log\left(\frac{H_\alpha}{H_\beta}\right)$ shown on the abscissa. 100 random states from the MCMC chain plotted in blue. Measurements of $\log(M_{H_2})$ are shown in red

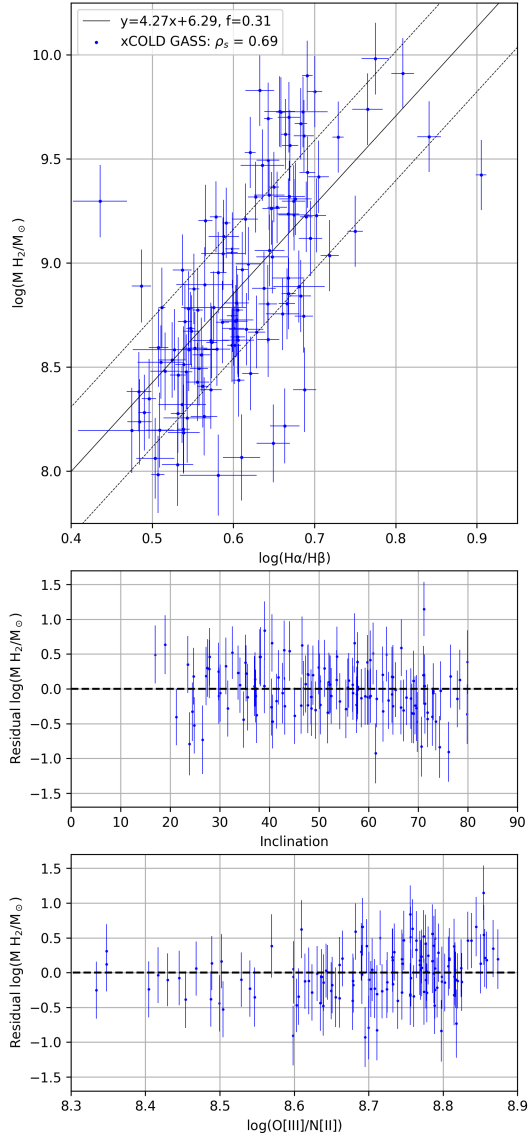


Figure 4.11 Relationships between $\log(M_{H_2})$ and the Balmer decrement constrained using median MCMC values the xCOLD sampled set.

In figure 4.11, the xCOLD GASS sample and calibrator are displayed. The intrinsic

scatter of the relation is shown with the dashed line. In the lower two sub-figures of figure 4.11, the dependencies of residual values in comparison to inclination and metallicity ($\log(\frac{O[III]}{N[II]})$) are examined within the xCOLD GASS sample. Residuals show no direct correlation with inclination. Additionally, residual values show no direct correlation with metallicity.

The main factor in determining the conversion factor α_{CO} for use in transforming $\log(L_{CO_{1 \rightarrow 0}})$ to $\log(M_{H_2})$ is metallicity(78). The dependency on metallicity for the $\log(L_{CO_{1 \rightarrow 0}})$ calibration (figure 4.7) is no longer present in the calibration of $\log(M_{H_2})$ (figure 4.11).

4.2.4 Dust Mass

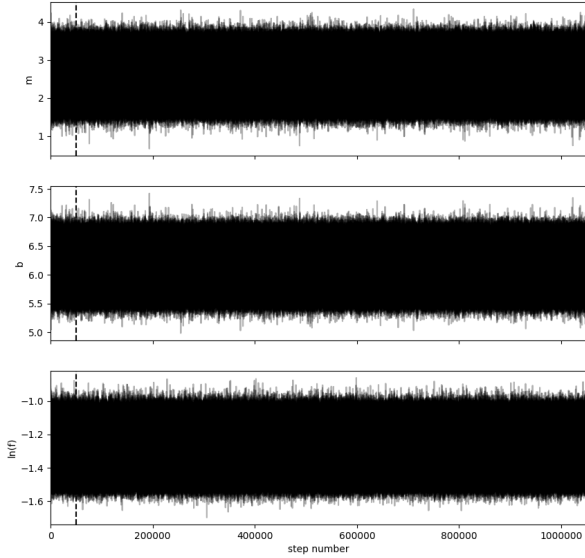


Figure 4.12 The converged Markov chains of the parameters of the Balmer decrement and $\log(M_{Dust})$ relation. The dashed vertical line denotes the end of the burn-in period, which was 5×10^4 steps

In calibrating $\log(M_{Dust})$, the intrinsic scatter f was lower than both the $\log(L_{CO_{1 \rightarrow 0}})$ and $\log(M_{H_2})$ calibrations. This calibration was the best constrained, with the lowest 1σ values for b and m (table 4.2).

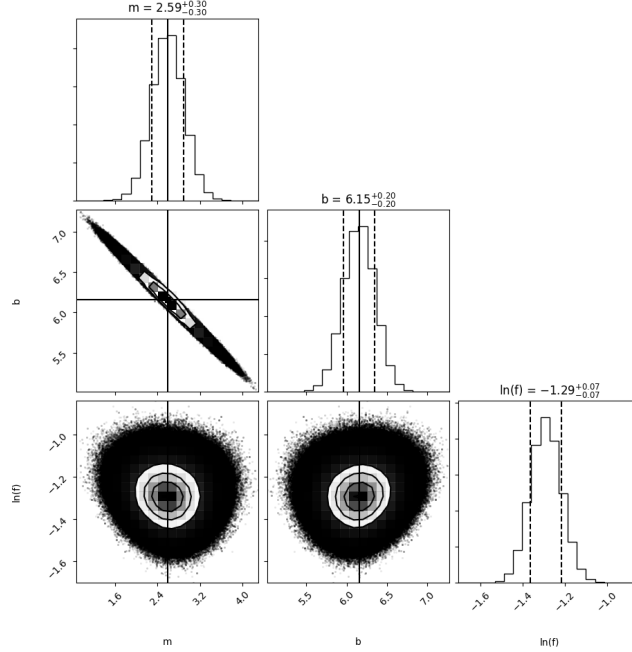


Figure 4.13 The resulting distributions from the chains in figure 4.12, showing the median and $1-\sigma$ (gaussian) standard deviation for each parameter. The MCMC algorithm calculates the scatter in terms of the natural log, $\ln(f)$. When converted to log-log scale, the scatter $f = 0.28$

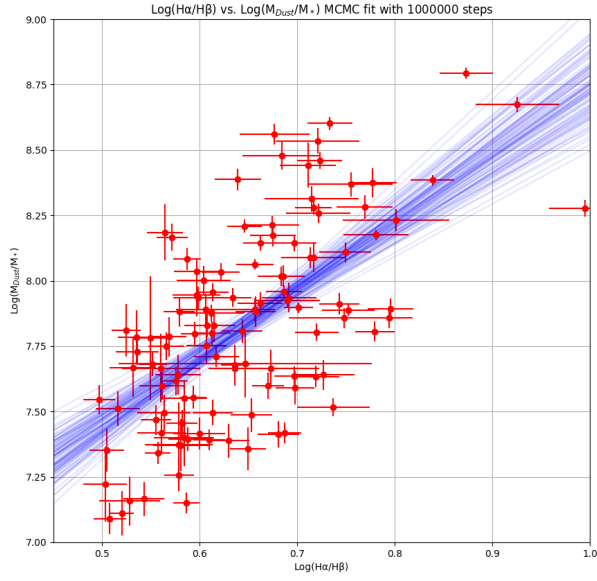


Figure 4.14 $\log(M_{Dust})$ shown on ordinate, $\log\left(\frac{H\alpha}{H\beta}\right)$ shown on the abscissa. 100 random states from the MCMC chain plotted in blue. Measurements of $\log\left(\frac{H\alpha}{H\beta}\right)$ are shown in red.

In figure 4.15, the JINGLE sample and calibrator are displayed. The intrinsic scatter of the relation is shown with the dashed line. In the lower two sub-figures of figure 4.15, the dependencies of residual values in comparison to inclination and metallicity ($\log\left(\frac{O[II]}{N[II]}\right)$) are examined within the JINGLE sample. In both sub-figures, no significant trend emerges between galactic inclination and residual $\log(M_{Dust})$.

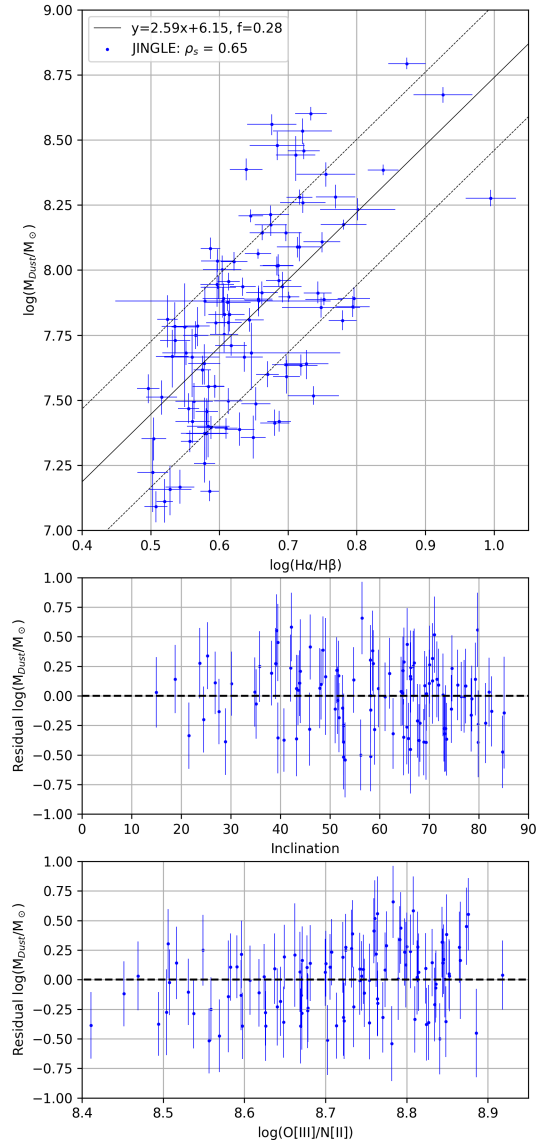


Figure 4.15 Relationships between $\log(M_{Dust})$ and the Balmer decrement constrained using median MCMC values the JINGLE sampled set.

4.2.5 MCMC results

Matter component	m	$1\sigma_m$	b	$1\sigma_b$	$\ln(f)$	$1\sigma_{\ln(f)}$	f	$1\sigma_f$
$\log(L_{CO_{1 \rightarrow 0}})$	5.89	0.53	4.59	0.33	-0.83	0.07	0.44	1.07
$\log(M_{H_2})$	4.27	0.42	6.29	0.26	-1.16	0.11	0.31	1.12
$\log(M_{Dust})$	2.59	0.3	6.15	0.2	-1.29	0.07	0.28	1.07

Table 4.2 MCMC parameters from the 10^6 step chain over $\log(L_{CO_{1 \rightarrow 0}})$, $\log(M_{H_2})$ (xCOLD GASS), and $\log(M_{Dust})$ (JINGLE). m , b , and $\ln(f)$ were selected as the median value of the chain density distribution. The MCMC chain obtained the natural logarithm of the scatter, $\ln(f)$. To accurately represent scatter between $\log(\frac{H_\alpha}{H_\beta})$ and the log of the matter component, $f = e^{\ln(f)}$ was used to transform $\ln(f)$ to f . The appropriate values for f and $1\sigma_f$ are provided in the final 2 columns.

4.3 Applying the Calibration: SDSS

The results from table 4.2 can be applied to a wider sample of galaxies that fit the same criteria (section 4.1). Of the 927,552 galaxies in the SDSS DR-7 sample(89), 54,465 are classified as star-forming galaxies with Balmer decrement signal-to-noise ratios above 5. The full distribution of galaxies in the $\log(SFR) - M_*$ plane is shown in figure 4.16.

Statistical tests can be performed on the SDSS sample with applied calibrators. By

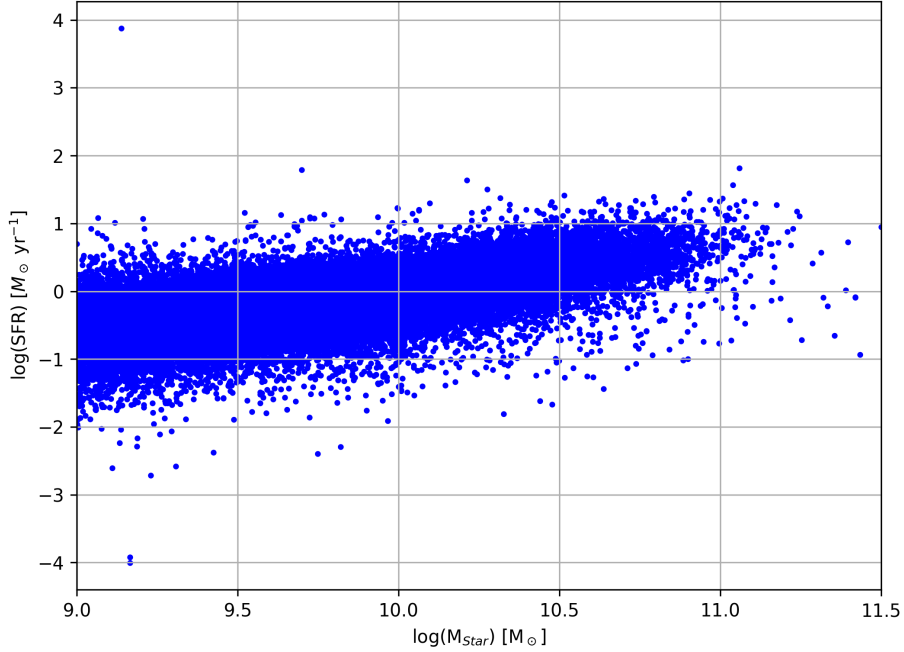


Figure 4.16 Distribution of the SDSS galaxies within the SFR- M_* plane.

probing the galaxies outside of the 1σ confidence interval of certain parameters allows for examination of the most extreme subsets of these galaxies. The main parameter selected to probe the extreme galactic subsets was inclination. Galaxies with higher inclinations should have amplified extinction effects, as observations of galaxies are made through higher concentrations of the galactic disk. At higher inclinations, the effects of extinction should be higher for measurements of $\log\left(\frac{H\alpha}{H\beta}\right)$, and any biases in the calibration should emerge as a result.

Within the full SDSS galaxy sample, galaxies with $i \geq 73^\circ$ fall outside of the 1σ distribution of inclination values, forming the upper subset of galaxies with the most extreme inclination effects. Galaxies with $i \leq 36^\circ$ fall outside of the 1σ distribution of inclination values, forming the lower subset of galaxies with the lowest inclination effects. These subsets establish the most extreme subsets of extinction processes, where

biases in the calibration of $\log(M_{H_2})$ and $\log(M_{Dust})$ would be the most prevalent. The distribution of these subsets in the $\log(SFR) - M_*$ plane is shown in lower-right sub-figure of figure 4.16. The subsets occupy similar regions in the $\log(SFR) - M_*$ plane, still encompassing the full array of types of star forming galaxies.

4.3.1 Molecular gas

Applying the results from table 4.2 to the SDSS sample, the molecular gas content can be calculated. The distribution of the molecular gas content in the $\log(SFR) - M_*$ plane is shown in figure 4.17.

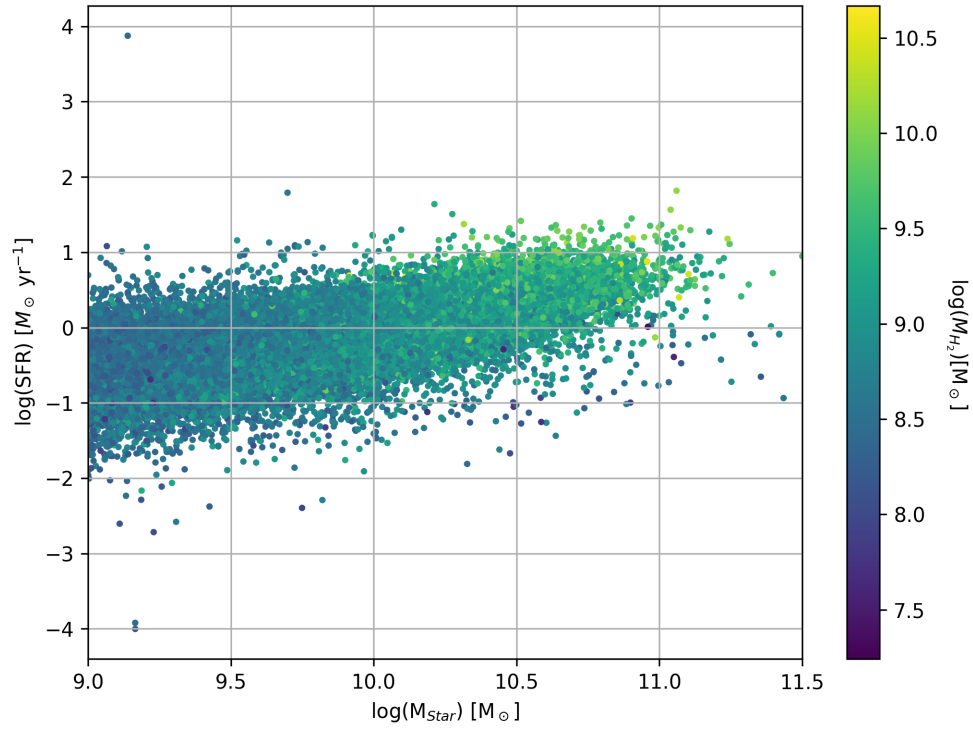


Figure 4.17 Distribution of the SDSS sample in the SFR- M_* plane, colorized by $\log(M_{H_2})$

Figure 4.17 shows two separate trends with the calibrator. In general, higher mass systems exhibit higher molecular gas content. This is an expected result. For high mass systems ($\log M \geq 10M_{\odot}$), galaxies with higher star formation rates have higher molecular gas content. This is an expected result, as galaxies with higher star forming resources have higher star formation rates. This trend should be present in lower mass systems. Despite no obvious trend in the lower mass systems, further analysis of star formation trends is necessary.

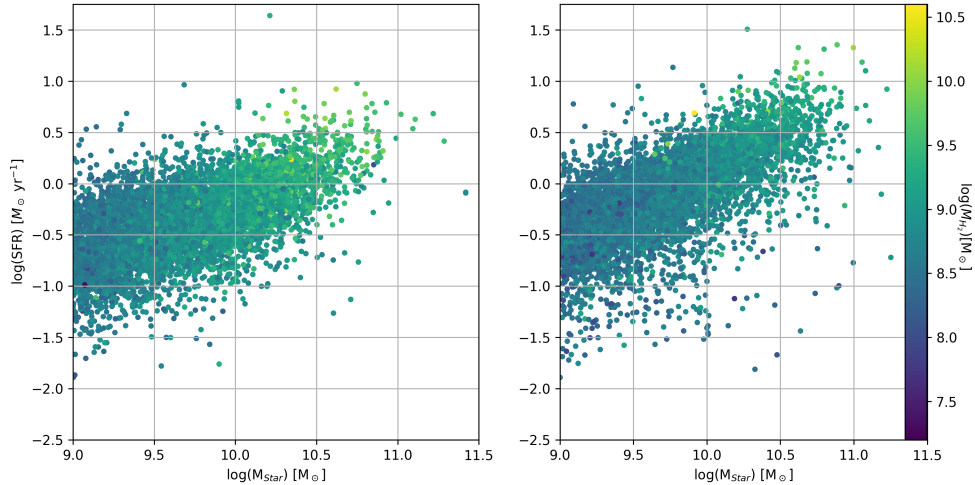


Figure 4.18 Distribution of SDSS sample in the SFR- M_{\star} plane, colorized by $\log(M_{H_2})$. The left figure displays galaxies with $i \geq 73^{\circ}$. The right figure displays galaxies with $i \leq 36^{\circ}$.

The distribution of galaxies with high inclination ($i \geq 73^{\circ}$) and low inclination ($i \leq 36^{\circ}$) are shown within figure 4.18. These subsets show the effects of inclination dependent reddening in figure 4.18. Galaxies at high inclination are effected by dust and gas interactions. Observations of these galaxies are made through more of the galactic disk, and have higher extinction effects on the Balmer emission. This appears in the inclination separation as higher relative gas content in the subset of high inclinations, and lower relative gas content in the subset of low inclinations.

Gas Fraction

To accurately calculate the gas-fraction of galaxies given a measure of the $\log(M_{H_2})$ within them, the stellar mass and molecular gas-mass must be converted into natural numbers before calculation of f_{H_2} .

$$\log(f_{H_2}) = \log\left(\frac{10^{\log(M_{H_2})}}{10^{\log(M_*)}}\right) \quad (4.2)$$

Using the prescription defined in equation 4.2, the gas fraction of galaxies in the $\log(SFR) - M_*$ plane can be explored.

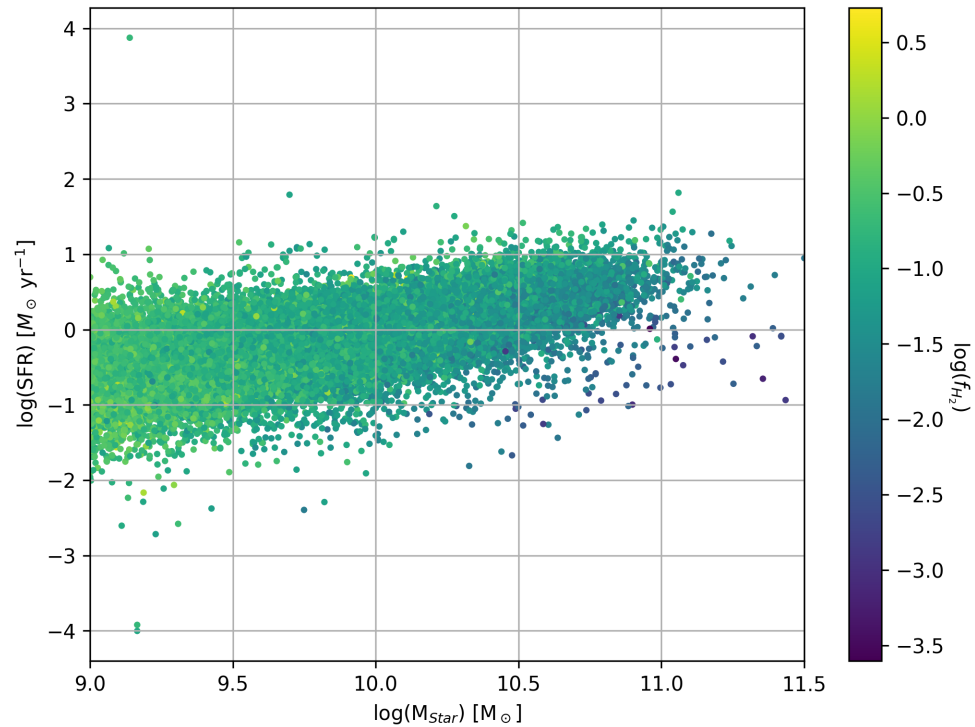


Figure 4.19 Distribution of the SDSS sample in the SFR- M_* plane, colorized by $\log(f_{H_2})$

Similar to the results from figure 4.17, figure 4.19 shows a strong trend between $\log(f_{H_2})$ and the stellar mass. Additionally, $\log(f_{H_2})$ is correlated to star-formation rates in high-mass galaxies.

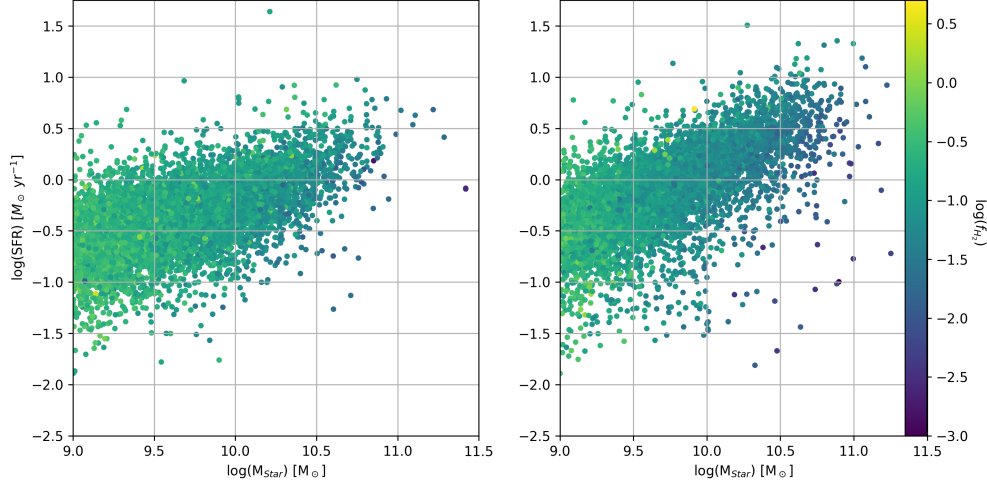


Figure 4.20 Distribution of SDSS sample in the SFR- M_* plane, colorized by $\log(f_{H_2})$. The left figure displays galaxies with $i \geq 73^\circ$. The right figure displays galaxies with $i \leq 36^\circ$.

The high and low inclination sub-sets mirror shown in figure 4.20 again mirror the results shown in figure 4.18. The high inclination subset wears the effects of interstellar reddening, which result in higher observed values of $\frac{F_{H\alpha}}{F_{H\beta}}$. This effects the calibration by

4.3.2 Dust Mass

The calibrators from table 4.2 were used to calculate dust masses within galaxies from the SDSS sample. The distribution of galaxies in the $\log(SFR) - M_*$ plane is shown in figure 4.21 with the dust content of each galaxy represented by the color. Figure 4.21 shows a strong trend between the stellar mass and the dust-content of

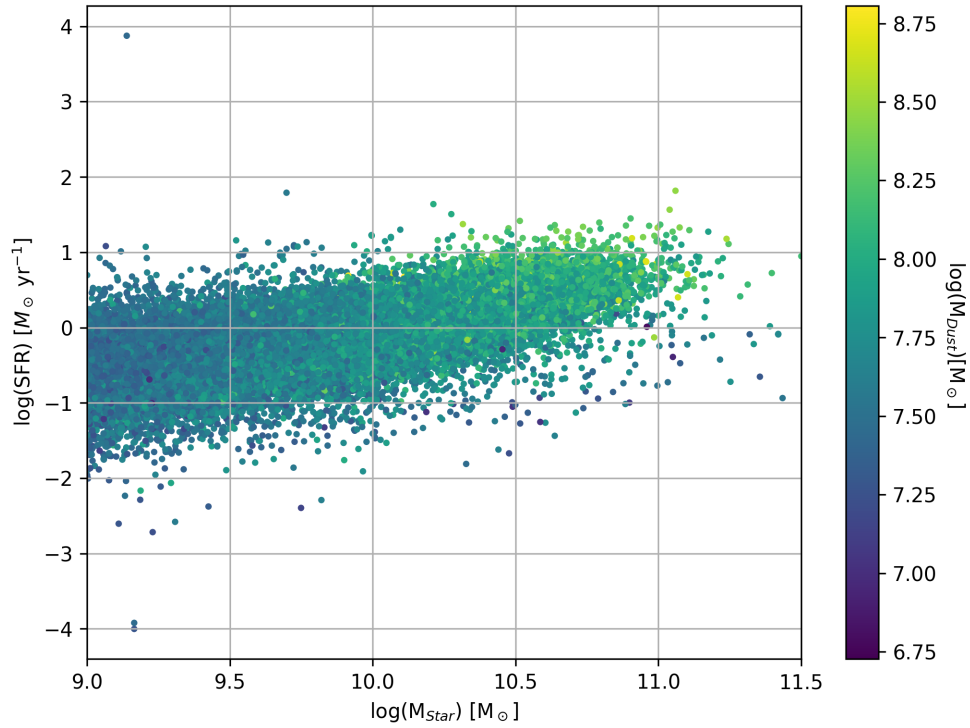


Figure 4.21 Distribution of the SDSS sample in the SFR- M_* plane, colorized by $\log(M_{\text{Dust}})$

the galaxy. In addition, high mass systems ($\log M \geq 10 M_{\odot}$) show strong correlations to high dust content in galaxies with high star formation rates.

Ample evidence exists for sites of dust formation in the stellar outflows of young stars(92). Therefore, areas of high star formation should exhibit higher dust content than low star-formation regions. This is supported by figure 4.21, with higher dust content in galaxies with high star formation rates. However, this is only apparent in high mass systems ($\log M \geq 10 M_{\odot}$), and further analysis of star formation trends is required in order to further reveal the complex relationship.

Figure 4.22 shows the galaxy subsets of extreme inclination. These subsets have $i \geq 73^{\circ}$ and $i \leq 36^{\circ}$. The effects of inclination dependent reddening on the calibrator

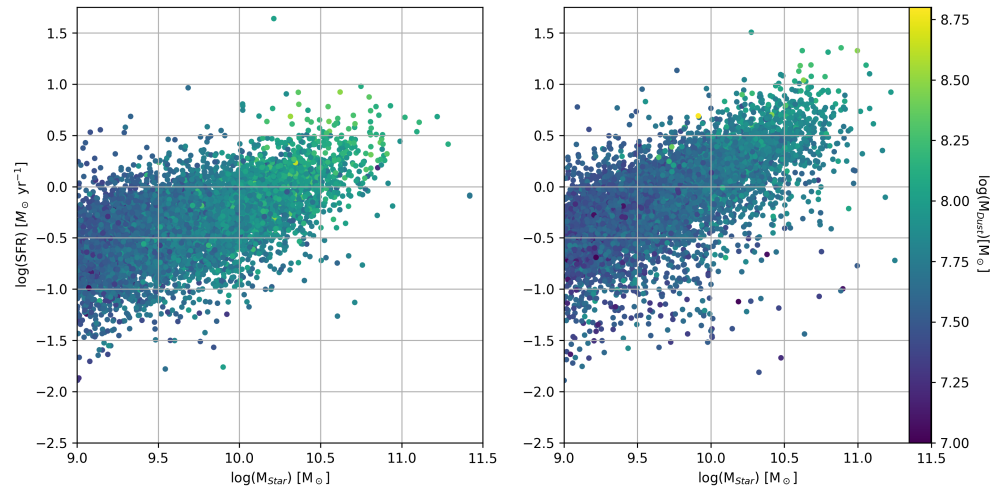


Figure 4.22 Distribution of SDSS sample in the SFR- M_* plane, colorized by $\log(M_{\text{Dust}})$. The left figure displays galaxies with $i \geq 73^\circ$. The right figure displays galaxies with $i \leq 36^\circ$.

are evident within figure 4.21. The subset of higher inclinations shows a higher relative dust content when compared to galaxies of similar stellar mass and star formation rate.

Chapter 5

Conclusion

By selecting a sample of star-forming galaxies with accurate measures of dust and cold-gas content, the relationship between the matter component and the Balmer decrement can be constrained. The calibration finds a dependence on metallicity when constraining $\log(L_{CO_{1\rightarrow 0}})$. The metallicity dependence is removed when constraining the cold-gas component, similar to the adjustments made in the original sample measurement(78). The cold-gas calibration is effected by inclination dependent reddening, and this is evident when the calibrator is applied to a wider galaxy sample. The dust calibration shows no dependence on metallicity, but exhibits a dependence on inclination when applied to a wider galaxy sample.

Applying the results of each calibrator (table 4.2) to a survey of galaxies with precise $H\alpha$ and $H\beta$ measurements allows for a test of the calibrations within the $\log(SFR) - M_*$ plane. Within the full SDSS sample, the cold-gas and dust content are in high abundance in galaxies with high star formation rates and high stellar mass. Figures 4.17 and 4.21 illustrate the accurate distribution of cold-gas and dust within the $\log(SFR) - M_*$ plane. The calibrations of cold-gas and dust are well constrained, but

are affected by inclination dependent reddening. This is evident when investigating galaxies in the SDSS sample with higher and lower values of inclination. In order to further constrain the dust and cold-gas content, the effects of inclinatiton must be accounted for. Moving forward, a further implementation of MCMC methods incorporating the effects of inclination (i) would result in a better constrained calibration.

$$M_{H_2,Dust} = m_1 \times \log\left(\frac{H\alpha}{H\beta}\right) + m_2 \times (i) + b \quad (5.1)$$

Star-forming galaxies are selected due to the lack of impact of the galactic core on $H\alpha$ and $H\beta$ emission. Passive galaxies do not have strong Balmer emission, while the Balmer emission from galaxies with an active galactic nucleus is effected by the galactic core. Within SDSS, star-forming galaxies comprise 26.6% of the galaxies in the entire survey(91). The sub-sample of star-forming galaxies is a predominant classification within the wider SDSS sample, and conclusions about the gas and dust content of the sub-sample is necessary to help construct the full picture of the baryonic matter content in galaxies.

Within any galaxy, the baryonic content can be separated into principal components: stars, gas, and dust. Gas can be further partitioned by its state: atomic and molecular. Within this study, constraints on the molecular state have been determined. The atomic state can be probed through the two sub-states of ionized and neutral atomic hydrogen. Neutral atomic hydrogen can be detected through the 21-cm spin-flip transition of hydrogen, which can be used in concordance with luminosity profiles to construct a mass function(93). The abundance of $\frac{\Omega_{H_2}}{\Omega_{HI}}$ is weakly correlated in the local universe, varying for nearby galaxies(94). Detection of atomic ionized hydrogen relies on $H\alpha$ emission, and are confined to spiral, star-forming galaxies(95). While H II regions are small in total mass, H II traces the star formation regions in a galaxy.

H II regions are an important component in the star-formation processes in a galaxy. Bringing together each of these gaseous elements allows for a better picture of the gas content of galaxies as a whole. Fully calibrating the gas content of star-forming galaxies in the local universe would be the first step in understanding the full baryonic matter budget of these galaxies.

While this study has focused primarily on baryonic matter, it is not the only type of matter in galaxies. Baryonic matter mass is small in comparison to the total mass of a galaxy system. Dark matter composes most of the mass in a galaxy system. Despite tremendous abundance, the lack of a direct observational signature presents problems with the detection of dark matter. However, using observation of the galaxies that host dark matter can allow for inference on the dark-matter content within them.

There are currently several surveys that are investigating the dark-matter distribution in galaxies. The Dark Energy Spectroscopy Instrument (DESI) will perform a survey of galaxies and quasars from 2020-2025 to construct a map of the underlying structure distribution(96). The overall focus of the DESI survey is to map the large-scale structure of the universe to constrain models of dark energy. Another primary goal is to determine the total amount of mass in the large scale structure of the universe.

When the redshift of any object is measured, there are two contributions to that measurement. There is a large contribution to the redshift from the cosmological expansion of the universe, and a smaller contribution coming from the gravitational interaction in the surrounding large scale structure. The smaller component is often called peculiar velocity. In measuring the peculiar velocity, the total mass of the system can be derived. The total mass of the system includes this dark matter mass. This observational effect is called redshift space distortions(97).

While the total mass of gas and dust in the context of galaxies is quite small, the im-

portance of these components in the formation of stars and the effect on observations cannot be undersold. A union of dust and cold gas calibrations with measurements of the other baryonic components allows for a complete picture of the baryonic content in a galaxy. With the commencement of new astronomical surveys providing prospects on calibrating dark matter content in the universe, it is possible to construct a description of the total matter composition of galaxies with respect to both baryonic and non-baryonic components.

Appendix

All of the blood, sweat, and codes generated throughout this project will be made available in a github respository on my github here: github.com/seanmacb

List of Figures

1.1	The 2018 Planck map of the polarized CMB anisotropies, shown as rods whose direction and length represent the direction and amplitude of polarized CMB. The colored background is the map of intensity anisotropies, smoothed to 5 degrees (1). Simply put, this is a map of the earliest light we can observe.	6
2.1	Luminosity of light emitted at different wavelengths from a blackbody at different temperatures according to Planck's Law (2.1).	11
2.2	Spectra of the galaxy J131721.28+310334.1 obtained using SDSS DR-16. This galaxy is a star forming galaxy at $Z = 0.019$ and is a member of the JINGLE survey. This spectrum is of an older galaxy of the galaxies within this survey. Absorption (blue) and emission (red) from elements are labeled within the spectrum.	12
2.3	Schematic of the CCD camera used by the Sloan digital sky survey (SDSS)(13).	15

2.4	Composite images of Barnard-68. Barnard-68 is a dense molecular cloud within the milky way made of dense, cold gas and dust. The cloud is opaque at visible wavelengths, but is shielding over 1,000 background Milky Way stars which can be observed in the infrared(14).	16
2.5	The wavelength-dependent relationship between absolute extinction $\frac{A(\lambda)}{A(V)}$ of visible and near infrared light. Observational evidence indicates extinction processes are more efficient on higher energy light(16).	17
2.6	A colormap showing how R_V and $E(B-V)$ affect the balmer decrement of a source. As $\lambda_\alpha(656.56nm) > \lambda_\beta(486.13nm) \rightarrow E \propto \frac{1}{\lambda}$, therefore $E_\alpha < E_\beta \ \& \ A_\alpha < A_\beta$. This functional relationship means $\frac{H_\alpha}{H_\beta}$ will be higher in environments with higher extinction.	20
2.7	Applying equation 2.9 for fixed values of $E(B - V)$ and allowing R_V to vary continuously shows that higher values of $E(B - V)$ results in higher values of $\frac{H_\alpha}{H_\beta}$	20
2.8	Applying equation 2.9 for fixed values of R_V and allowing $E(B - V)$ to vary continuously shows that higher values of R_V result in higher values of $\frac{H_\alpha}{H_\beta}$	20
2.9	Rotation curve of the Andromeda galaxy obtained using an image tube spectrograph by Vera Rubin and Kent Ford(23). This result was in direct contrast to the expected rotation curve of a galaxy which should decrease $\propto \frac{1}{r^2}$ if the galactic disk were the only mass component at large radii.	23

2.10 The bullet cluster, shown with X-ray flux from baryonic gas content in pink, and the total matter density reconstructed from weak gravitational lensing(24)	25
2.11 M87(36)	30
2.12 M89(37)	30
2.13 ESO 325-G004(38)	30
2.14 The Faber-Jackson relation describing the luminosity of elliptical galaxies versus the central stellar velocity dispersion(44)	31
2.15 NGC 2787 (NASA Hubble)	33
2.16 NGC 6861 (NASA Hubble)	33
2.17 NGC 5866 (NASA Hubble)	33
2.18 Pinwheel Galaxy (NASA/ESA)	34
2.19 NGC 5055 (NASA/ESA)	34
2.20 Andromeda Galaxy (NASA/ESA)	34
2.21 The Tully-Fisher relation for spiral galaxies using results from the GHASP sample, which follows $M_{bar} = 10^{2.21 \pm 0.61} V_{max}^{3.64 \pm 0.28}$ (57)	35
2.22 A map of our home galaxy, the Milky Way(66). The central bar and different spiral arms are the defining features of the spiral structure of the Milky Way.	36

2.23		
NGC 2623 (NASA Hubble)	38	
2.24		
Antennae Galaxies (NASA Hubble)	38	
2.25		
Mice Galaxies (NASA Hubble)	38	
3.1	A plot detailing how the prior ($N(\mu = -0.15, \sigma = 0.5)$) and likelihood ($N(\mu = 0.1, \sigma = 0.1)$) probability distributions affect the posterior distribution	42
3.2	Figure from (84) showing the star-formation stellar mass plane. Galaxies that are actively forming stars are classified as main sequence star-forming galaxies. As galaxies exhaust their star-forming resources, the star-formation rate of the galaxy decreases. Galaxies in this later evolutionary stage of evolution are in the lower group of galaxies.	45
3.3	Calibrated α_{CO} conversion function with independent calibration from molecular gas depletion timescale(85)	45
3.4	Examples of an SED of one galaxy in the JINGLE sample(79), fitted with the single-modified black body (SMBB, left), the broken emissivity law modified black-body (BMBB, middle), and the two modified black-bodies (TMBB, right) models.	46

4.1	Histograms detailing the distribution of SDSS galaxy sample after data reduction. Histograms show galaxy redshift (Z), stellar mass ($\log\left(\frac{M}{M_\odot}\right)$), and E(B-V) color	49
4.2	Histograms detailing the distribution of JINGLE galaxy samples used for MCMC calibration. Histograms detail galaxy redshift (Z), stellar mass ($\log\left(\frac{M}{M_\odot}\right)$), and FUV-K color	50
4.3	Histograms detailing the distribution of xCOLD GASS galaxy samples. Histograms detail galaxy redshift (Z), stellar mass ($\log\left(\frac{M}{M_\odot}\right)$), and NUV-R color	51
4.4	The converged Markov chains of the parameters of the Balmer decrement and LCO_{1-0} relation. The dashed vertical line denotes the end of the burn-in period, which was 50,000 steps	53
4.5	The resulting distributions from the chains in figure 4.4, showing the median and $1-\sigma$ (gaussian) standard deviation for each parameter. The MCMC algorithm calculates the scatter in terms of the natural log of the scatter, $\ln(f)$. When converted to log-log scale, the scatter $f = 0.44$	54
4.6	$\log(L_{CO_{1 \rightarrow 0}})$ shown on ordinate, $\log\left(\frac{H\alpha}{H\beta}\right)$ shown on the abscissa. 100 random states from the MCMC chain plotted in blue. Measurements of $\log(L_{CO_{1 \rightarrow 0}})$ are shown in red.	55
4.7	Relationships between $\log(L_{CO_{1 \rightarrow 0}})$ and the Balmer decrement constrained using median MCMC values the xCOLD sampled set.	56

4.8	The converged Markov chains of the parameters of the Balmer decrement and $\log(M_{H_2})$ relation. The dashed vertical line denotes the end of the burn-in period, which was 50,000 steps	58
4.9	The resulting distributions from the chains in figure 4.8, showing the median and $1-\sigma$ (gaussian) standard deviation for each parameter. The MCMC algorithm calculates the scatter in terms of the natural log, $\ln(f)$. When converted to log-log scale, the scatter $f = 0.31$	59
4.10	$\log(M_{H_2})$ shown on the ordinate, $\log\left(\frac{H_\alpha}{H_\beta}\right)$ shown on the abscissa. 100 random states from the MCMC chain plotted in blue. Measurements of $\log(M_{H_2})$ are shown in red	60
4.11	Relationships between $\log(M_{H_2})$ and the Balmer decrement constrained using median MCMC values the xCOLD sampled set.	61
4.12	The converged Markov chains of the parameters of the Balmer decrement and $\log(M_{Dust})$ relation. The dashed vertical line denotes the end of the burn-in period, which was 5×10^4 steps	62
4.13	The resulting distributions from the chains in figure 4.12, showing the median and $1-\sigma$ (gaussian) standard deviation for each parameter. The MCMC algorithm calculates the scatter in terms of the natural log, $\ln(f)$. When converted to log-log scale, the scatter $f = 0.28$	63
4.14	$\log(M_{Dust})$ shown on ordinate, $\log\left(\frac{H_\alpha}{H_\beta}\right)$ shown on the abscissa. 100 random states from the MCMC chain plotted in blue. Measurements of $\log\left(\frac{H_\alpha}{H_\beta}\right)$ are shown in red.	64

4.15 Relationships between $\log(M_{Dust})$ and the Balmer decrement constrained using median MCMC values the JINGLE sampled set.	65
4.16 Distribution of the SDSS galaxies within the SFR- M_* plane.	67
4.17 Distribution of the SDSS sample in the SFR- M_* plane, colorized by $\log(M_{H_2})$	68
4.18 Distribution of SDSS sample in the SFR- M_* plane, colorized by $\log(M_{H_2})$. The left figure displays galaxies with $i \geq 73^\circ$. The right figure displays galaxies with $i \leq 36^\circ$	69
4.19 Distribution of the SDSS sample in the SFR- M_* plane, colorized by $\log(f_{H_2})$	70
4.20 Distribution of SDSS sample in the SFR- M_* plane, colorized by $\log(f_{H_2})$. The left figure displays galaxies with $i \geq 73^\circ$. The right figure displays galaxies with $i \leq 36^\circ$	71
4.21 Distribution of the SDSS sample in the SFR- M_* plane, colorized by $\log(M_{Dust})$	72
4.22 Distribution of SDSS sample in the SFR- M_* plane, colorized by $\log(M_{Dust})$. The left figure displays galaxies with $i \geq 73^\circ$. The right figure displays galaxies with $i \leq 36^\circ$	73

Bibliography

- [1] Planck Collaboration, N. Aghanim, Y. Akrami, M. Ashdown, J. Aumont, C. Bacigalupi, M. Ballardini, A. J. Banday, R. B. Barreiro, N. Bartolo, S. Basak, R. Battye, K. Benabed, J. P. Bernard, M. Bersanelli, P. Bielewicz, J. J. Bock, J. R. Bond, J. Borrill, F. R. Bouchet, F. Boulanger, M. Bucher, C. Burigana, R. C. Butler, E. Calabrese, J. F. Cardoso, J. Carron, A. Challinor, H. C. Chiang, J. Chluba, L. P. L. Colombo, C. Combet, D. Contreras, B. P. Crill, F. Cuttaia, P. de Bernardis, G. de Zotti, J. Delabrouille, J. M. Delouis, E. Di Valentino, J. M. Diego, O. Doré, M. Douspis, A. Ducout, X. Dupac, S. Dusini, G. Efstathiou, F. Elsner, T. A. Enßlin, H. K. Eriksen, Y. Fantaye, M. Farhang, J. Fergusson, R. Fernandez-Cobos, F. Finelli, F. Forastieri, M. Frailis, A. A. Fraisse, E. Franceschi, A. Frolov, S. Galeotta, S. Galli, K. Ganga, R. T. Génova-Santos, M. Gerbino, T. Ghosh, J. González-Nuevo, K. M. Górski, S. Gratton, A. Grupuso, J. E. Gudmundsson, J. Hamann, W. Handley, F. K. Hansen, D. Herranz, S. R. Hildebrandt, E. Hivon, Z. Huang, A. H. Jaffe, W. C. Jones, A. Karakci, E. Keihänen, R. Kesktalo, K. Kiiveri, J. Kim, T. S. Kisner, L. Knox, N. Krachmalnicoff, M. Kunz, H. Kurki-Suonio, G. Lagache, J. M. Lamarre, A. Lasenby, M. Lattanzi, C. R. Lawrence, M. Le Jeune, P. Lemos, J. Lesgourgues, F. Levrier, A. Lewis, M. Liguori, P. B. Lilje, M. Lilley, V. Lindholm, M. López-Caniego, P. M. Lubin, Y. Z. Ma, J. F. Macías-Pérez, G. Maggio, D. Maino, N. Mandlesi, A. Mangilli, A. Marcos-Caballero, M. Maris, P. G. Martin, M. Martinelli,

E. Martínez-González, S. Matarrese, N. Mauri, J. D. McEwen, P. R. Meinhold, A. Melchiorri, A. Mennella, M. Migliaccio, M. Millea, S. Mitra, M. A. Miville-Deschénes, D. Molinari, L. Montier, G. Morgante, A. Moss, P. Natoli, H. U. Nørgaard-Nielsen, L. Pagano, D. Paoletti, B. Partridge, G. Patanchon, H. V. Peiris, F. Perrotta, V. Pettorino, F. Piacentini, L. Polastri, G. Polenta, J. L. Puget, J. P. Rachen, M. Reinecke, M. Remazeilles, A. Renzi, G. Rocha, C. Rosset, G. Roudier, J. A. Rubiño-Martín, B. Ruiz-Granados, L. Salvati, M. Sandri, M. Savelainen, D. Scott, E. P. S. Shellard, C. Sirignano, G. Sirri, L. D. Spencer, R. Sunyaev, A. S. Suur-Uski, J. A. Tauber, D. Tavagnacco, M. Tenti, L. Toffolatti, M. Tomasi, T. Trombetti, L. Valenziano, J. Valiviita, B. Van Tent, L. Vibert, P. Vielva, F. Villa, N. Vittorio, B. Wandelt, I. K. Wehus, M. White, S. D. M. White, A. Zacc hei, and A. Zonca, “Planck 2018 results. VI. Cosmological parameters,” *arXiv e-prints*, p. arXiv:1807.06209, July 2018.

- [2] M. L. Kutner, *Astronomy: A Physical Perspective*. 2003.
- [3] J. O. Bennett, M. Donahue, N. Schneider, and M. Voit, *The Cosmic Perspective*. 2004.
- [4] A. D. Sakharov, “Violation of CP Invariance, C Asymmetry, and Baryon Asymmetry of the Universe,” *Soviet Journal of Experimental and Theoretical Physics Letters*, vol. 5, p. 24, Jan. 1967.
- [5] B. Ryden, *Introduction to cosmology*. 2003.
- [6] Planck Collaboration, P. A. R. Ade, N. Aghanim, M. Arnaud, M. Ashdown, J. Aumont, C. Baccigalupi, A. J. Banday, R. B. Barreiro, J. G. Bartlett, N. Bartolo, E. Battaner, R. Battye, K. Benabed, A. Benoît, A. Benoit-Lévy, J. P. Bernard, M. Bersanelli, P. Bielewicz, J. J. Bock, A. Bonaldi, L. Bonavera, J. R. Bond, J. Borrill, F. R. Bouchet, F. Boulanger, M. Bucher, C. Burigana, R. C.

Butler, E. Calabrese, J. F. Cardoso, A. Catalano, A. Challinor, A. Chamballu, R. R. Chary, H. C. Chiang, J. Chluba, P. R. Christensen, S. Church, D. L. Clements, S. Colombi, L. P. L. Colombo, C. Combet, A. Coulais, B. P. Crill, A. Curto, F. Cuttaia, L. Danese, R. D. Davies, R. J. Davis, P. de Bernardis, A. de Rosa, G. de Zotti, J. Delabrouille, F. X. Désert, E. Di Valentino, C. Dickinson, J. M. Diego, K. Dolag, H. Dole, S. Donzelli, O. Doré, M. Douspis, A. Ducout, J. Dunkley, X. Dupac, G. Efstathiou, F. Elsner, T. A. Enßlin, H. K. Eriksen, M. Farhang, J. Fergusson, F. Finelli, O. Forni, M. Frailis, A. A. Fraisse, E. Franceschi, A. Frejsel, S. Galeotta, S. Galli, K. Ganga, C. Gauthier, M. Gerbino, T. Ghosh, M. Giard, Y. Giraud-Héraud, E. Giusarma, E. Gjerløw, J. González-Nuevo, K. M. Górski, S. Gratton, A. Gregorio, A. Gruppuso, J. E. Guðmundsson, J. Hamann, F. K. Hansen, D. Hanson, D. L. Harrison, G. Helou, S. Henrot-Versillé, C. Hernández-Monteagudo, D. Herranz, S. R. Hildebrandt, E. Hivon, M. Hobson, W. A. Holmes, A. Hornstrup, W. Hovest, Z. Huang, K. M. Huffenberger, G. Hurier, A. H. Jaffe, T. R. Jaffe, W. C. Jones, M. Juvela, E. Keihänen, R. Keskitalo, T. S. Kisner, R. Kneissl, J. Knoche, L. Knox, M. Kunz, H. Kurki-Suonio, G. Lagache, A. Lähteenmäki, J. M. Lamarre, A. Lasenby, M. Lattanzi, C. R. Lawrence, J. P. Leahy, R. Leonardi, J. Lesgourges, F. Levrier, A. Lewis, M. Liguori, P. B. Lilje, M. Linden-Vørnle, M. López-Caniego, P. M. Lubin, J. F. Macías-Pérez, G. Maggio, D. Maino, N. Mandlesi, A. Mangilli, A. Marchini, M. Maris, P. G. Martin, M. Martinelli, E. Martínez-González, S. Masi, S. Matarrese, P. McGehee, P. R. Meinhold, A. Melchiorri, J. B. Melin, L. Mendes, A. Mennella, M. Migliaccio, M. Millea, S. Mitra, M. A. Miville-Deschénes, A. Moneti, L. Montier, G. Morgante, D. Mortlock, A. Moss, D. Munshi, J. A. Murphy, P. Naselsky, F. Nati, P. Natoli, C. B. Netterfield, H. U. Nørgaard-Nielsen, F. Noviello, D. Novikov, I. Novikov, C. A. Oxborrow, F. Paci, L. Pagano, F. Pajot, R. Paladini, D. Paoletti, B. Partridge, F. Pasian,

G. Patanchon, T. J. Pearson, O. Perdereau, L. Perotto, F. Perrotta, V. Pettorino, F. Piacentini, M. Piat, E. Pierpaoli, D. Pietrobon, S. Plaszczynski, E. Pointecouteau, G. Polenta, L. Popa, G. W. Pratt, G. Prézeau, S. Prunet, J. L. Puget, J. P. Rachen, W. T. Reach, R. Rebolo, M. Reinecke, M. Remazeilles, C. Renault, A. Renzi, I. Ristorcelli, G. Rocha, C. Rosset, M. Rossetti, G. Roudier, B. Rouillé d'Orfeuil, M. Rowan-Robinson, J. A. Rubiño-Martín, B. Rusholme, N. Said, V. Salvatelli, L. Salvati, M. Sandri, D. Santos, M. Savelainen, G. Savini, D. Scott, M. D. Seiffert, P. Serra, E. P. S. Shellard, L. D. Spencer, M. Spinelli, V. Stolyarov, R. Stompor, R. Sudiwala, R. Sunyaev, D. Sutton, A. S. Suur-Uski, J. F. Sygnet, J. A. Tauber, L. Terenzi, L. Toffolatti, M. Tomasi, M. Tristram, T. Trombetti, M. Tucci, J. Tuovinen, M. Türler, G. Umana, L. Valenziano, J. Valiviita, F. Van Tent, P. Vielva, F. Villa, L. A. Wade, B. D. Wandelt, I. K. Wehus, M. White, S. D. M. White, A. Wilkinson, D. Yvon, A. Zacchei, and A. Zonca, “Planck 2015 results. XIII. Cosmological parameters,” , vol. 594, p. A13, Sept. 2016.

- [7] P. A. Oesch, G. Brammer, P. G. van Dokkum, G. D. Illingworth, R. J. Bouwens, I. Labb  , M. Franx, I. Momcheva, M. L. N. Ashby, G. G. Fazio, V. Gonzalez, B. Holden, D. Magee, R. E. Skelton, R. Smit, L. R. Spitler, M. Trenti, and S. P. Willner, “A Remarkably Luminous Galaxy at $z=11.1$ Measured with Hubble Space Telescope Grism Spectroscopy,” , vol. 819, p. 129, Mar. 2016.
- [8] S. D. M. White and M. J. Rees, “Core condensation in heavy halos: a two-stage theory for galaxy formation and clustering,” *Monthly Notices of the Royal Astronomical Society*, vol. 183, pp. 341–358, 07 1978.
- [9] B. T. Draine, “Interstellar Dust Grains,” , vol. 41, pp. 241–289, Jan. 2003.
- [10] M. Planck and M. Masius, *The Theory of Heat Radiation*. Blakiston, 1914.
- [11] A. Einstein, “Über einen die Erzeugung und Verwandlung des Lichtes betref-

fenden heuristischen Gesichtspunkt,” *Annalen der Physik*, vol. 322, pp. 132–148, Jan 1905.

- [12] H. Bradt, *Astrophysics Processes*. 2008.
- [13] J. E. Gunn, M. Carr, C. Rockosi, M. Sekiguchi, K. Berry, B. Elms, E. de Haas, Ž. . Ivezić, G. Knapp, R. Lupton, G. Pauls, R. Simcoe, R. Hirsch, D. Sanford, S. Wang, D. York, F. Harris, J. Annis, L. Bartozek, W. Boroski, J. Bakken, M. Haldeman, S. Kent, S. Holm, D. Holmgren, D. Petravick, A. Prosaio, R. Rechenmacher, M. Doi, M. Fukugita, K. Shimasaku, N. Okada, C. Hull, W. Siegmund, E. Mannery, M. Blouke, D. Heidtman, D. Schneider, R. Lucinio, and J. Brinkman, “The Sloan Digital Sky Survey Photometric Camera,” , vol. 116, pp. 3040–3081, Dec. 1998.
- [14] *The dark cloud B68 at different wavelengths*. Jul 1999.
- [15] G. S. Rossano, “Distribution of extinction in the Corona Australis dark cloud complex.,” , vol. 83, pp. 234–240, Mar. 1978.
- [16] J. A. Cardelli, G. C. Clayton, and J. S. Mathis, “The Relationship between Infrared, Optical, and Ultraviolet Extinction,” , vol. 345, p. 245, Oct 1989.
- [17] G. V. Schultz and W. Wiemer, “Interstellar reddening and IR-excesses of O and B stars.,” , vol. 43, pp. 133–139, Sept. 1975.
- [18] D. E. Osterbrock, *Astrophysics of gaseous nebulae and active galactic nuclei*. 1989.
- [19] R. C. Bohlin, B. D. Savage, and J. F. Drake, “A survey of interstellar H I from Lalpha absorption measurements. II.,” , vol. 224, pp. 132–142, Aug. 1978.
- [20] L. A. Valencic, G. C. Clayton, and K. D. Gordon, “Ultraviolet Extinction Properties in the Milky Way,” , vol. 616, pp. 912–924, Dec 2004.

- [21] G. C. Rudie, C. C. Steidel, A. E. Shapley, and M. Pettini, “The Column Density Distribution and Continuum Opacity of the Intergalactic and Circumgalactic Medium at Redshift $z = 2.4$,” , vol. 769, p. 146, June 2013.
- [22] F. Zwicky, “Die Rotverschiebung von extragalaktischen Nebeln,” *Helvetica Physica Acta*, vol. 6, pp. 110–127, Jan 1933.
- [23] V. C. Rubin and J. Ford, W. Kent, “Rotation of the Andromeda Nebula from a Spectroscopic Survey of Emission Regions,” , vol. 159, p. 379, Feb 1970.
- [24] M. Markevitch, A. H. Gonzalez, D. Clowe, A. Vikhlinin, W. Forman, C. Jones, S. Murray, and W. Tucker, “Direct Constraints on the Dark Matter Self-Interaction Cross Section from the Merging Galaxy Cluster 1E 0657-56,” , vol. 606, pp. 819–824, May 2004.
- [25] A. R. Liddle and D. H. Lyth, *Cosmological Inflation and Large-Scale Structure*. 2000.
- [26] P. Meszaros, “The behaviour of point masses in an expanding cosmological substratum.,” , vol. 37, pp. 225–228, Dec. 1974.
- [27] D. J. Eisenstein, I. Zehavi, D. W. Hogg, R. Scoccimarro, M. R. Blanton, R. C. Nichol, R. Scranton, H.-J. Seo, M. Tegmark, Z. Zheng, S. F. Anderson, J. Annis, N. Bahcall, J. Brinkmann, S. Burles, F. J. Castander, A. Connolly, I. Csabai, M. Doi, M. Fukugita, J. A. Frieman, K. Glazebrook, J. E. Gunn, J. S. Hendry, G. Hennessy, Z. Ivezić, S. Kent, G. R. Knapp, H. Lin, Y.-S. Loh, R. H. Lupton, B. Margon, T. A. McKay, A. Meiksin, J. A. Munn, A. Pope, M. W. Richmond, D. Schlegel, D. P. Schneider, K. Shimasaku, C. Stoughton, M. A. Strauss, M. SubbaRao, A. S. Szalay, I. Szapudi, D. L. Tucker, B. Yanny, and D. G. York, “Detection of the Baryon Acoustic Peak in the Large-Scale Correlation Function of SDSS Luminous Red Galaxies,” , vol. 633, pp. 560–574, Nov. 2005.

- [28] M. S. Longair, *Galaxy Formation*. 2008.
- [29] P. Norberg, C. M. Baugh, E. Hawkins, S. Maddox, D. Madgwick, O. Lahav, S. Cole, C. S. Frenk, I. Baldry, J. Bland -Hawthorn, T. Bridges, R. Cannon, M. Colless, C. Collins, W. Couch, G. Dalton, R. De Propris, S. P. Driver, G. Efstathiou, R. S. Ellis, K. Glazebrook, C. Jackson, I. Lewis, S. Lumsden, J. A. Peacock, B. A. Peterson, W. Sutherland, and K. Taylor, “The 2dF Galaxy Redshift Survey: the dependence of galaxy clustering on luminosity and spectral type,” , vol. 332, pp. 827–838, June 2002.
- [30] A. Leauthaud, M. R. George, P. S. Behroozi, K. Bundy, J. Tinker, R. H. Wechsler, C. Conroy, A. Finoguenov, and M. Tanaka, “The Integrated Stellar Content of Dark Matter Halos,” , vol. 746, p. 95, Feb. 2012.
- [31] S. D. M. White and M. J. Rees, “Core condensation in heavy halos: a two-stage theory for galaxy formation and clustering.,” , vol. 183, pp. 341–358, May 1978.
- [32] E. P. Hubble, “Cepheids in spiral nebulae,” *The Observatory*, vol. 48, pp. 139–142, May 1925.
- [33] E. P. Hubble, “The classification of spiral nebulae,” *The Observatory*, vol. 50, pp. 276–281, Sep 1927.
- [34] J. I. Read and N. Trentham, “The baryonic mass function of galaxies,” *Philosophical Transactions of the Royal Society of London Series A*, vol. 363, p. 2693, Dec 2005.
- [35] A. W. Graham and S. P. Driver, “A Concise Reference to (Projected) Sérsic $R^{1/n}$ Quantities, Including Concentration, Profile Slopes, Petrosian Indices, and Kron Magnitudes,” , vol. 22, pp. 118–127, Jan 2005.

- [36] This is the galactic core show as a composite image of visible and infrared observations in order to resolve the blue jet. The field of view is about 1.5 arc minutes across, the jet extends to about a third of an arc minute (or 20 arc seconds) with a width of about 2 arc seconds (absolute length 5 kly at a distance of 53 Mly). Aug 2009.
- [37] “Messier89 - hst - potw1902a.tif,” Jan 2019.
- [38] “Eso 325-g004,” Dec 2019.
- [39] J. Loveday, “The APM Bright Galaxy Catalogue,” , vol. 278, pp. 1025–1048, Feb 1996.
- [40] G. de Vaucouleurs, “Recherches sur les Nebuleuses Extragalactiques,” *Annales d’Astrophysique*, vol. 11, p. 247, Jan 1948.
- [41] J. Kormendy and S. Djorgovski, “Surface photometry and the structure of elliptical galaxies.,” , vol. 27, pp. 235–277, Jan. 1989.
- [42] T. R. Lauer, E. A. Ajhar, Y. I. Byun, A. Dressler, S. M. Faber, C. Grillmair, J. Kormendy, D. Richstone, and S. Tremaine, “The Centers of Early-Type Galaxies with HST.I.An Observational Survey,” , vol. 110, p. 2622, Dec. 1995.
- [43] J. Kormendy, D. B. Fisher, M. E. Cornell, and R. Bender, “Structure and Formation of Elliptical and Spheroidal Galaxies,” , vol. 182, pp. 216–309, May 2009.
- [44] S. M. Faber and R. E. Jackson, “Velocity dispersions and mass-to-light ratios for elliptical galaxies.,” , vol. 204, pp. 668–683, Mar. 1976.
- [45] M. Bernardi, J. B. Hyde, R. K. Sheth, C. J. Miller, and R. C. Nichol, “The Luminosities, Sizes, and Velocity Dispersions of Brightest Cluster Galaxies: Implications for Formation History,” , vol. 133, pp. 1741–1755, Apr. 2007.

- [46] R. Bender, D. Burstein, and S. M. Faber, “Dynamically Hot Galaxies. I. Structural Properties,” , vol. 399, p. 462, Nov. 1992.
- [47] M. Cappellari, E. Emsellem, R. Bacon, M. Bureau, R. L. Davies, P. T. de Zeeuw, J. Falcón-Barroso, D. Krajnović, H. Kuntschner, R. M. McDermid, R. F. Peletier, M. Sarzi, R. C. E. van den Bosch, and G. van de Ven, “The SAURON project - X. The orbital anisotropy of elliptical and lenticular galaxies: revisiting the $(V/\sigma, \epsilon)$ diagram with integral-field stellar kinematics,” , vol. 379, pp. 418–444, Aug. 2007.
- [48] D. Thomas, C. Maraston, R. Bender, and C. Mendes de Oliveira, “The Epochs of Early-Type Galaxy Formation as a Function of Environment,” , vol. 621, pp. 673–694, Mar. 2005.
- [49] A. Renzini, “Stellar Population Diagnostics of Elliptical Galaxy Formation,” , vol. 44, pp. 141–192, Sept. 2006.
- [50] S. M. Faber and J. S. Gallagher, “H I in early-type galaxies. II. Mass loss and galactic winds..,” , vol. 204, pp. 365–378, Mar. 1976.
- [51] G. R. Knapp, E. L. Turner, and P. E. Cunniffe, “The statistical distribution of the neutral-hydrogen content of elliptical galaxies.,” , vol. 90, pp. 454–468, Mar. 1985.
- [52] R. Morganti, P. T. de Zeeuw, T. A. Oosterloo, R. M. McDermid, D. Krajnović, M. Cappellari, F. Kenn, A. Weijmans, and M. Sarzi, “Neutral hydrogen in nearby elliptical and lenticular galaxies: the continuing formation of early-type galaxies,” , vol. 371, pp. 157–169, Sept. 2006.
- [53] L. M. Young, M. Bureau, and M. Cappellari, “Structure and Kinematics of Molecular Disks in Fast-Rotator Early-Type Galaxies,” , vol. 676, pp. 317–334, Mar. 2008.

- [54] N. Caldwell, J. A. Rose, R. M. Sharples, R. S. Ellis, and R. G. Bower, “Star Formation in Early-Type Galaxies in the Coma Cluster,” , vol. 106, p. 473, Aug 1993.
- [55] J. Binney and M. Merrifield, *Galactic Astronomy*. 1998.
- [56] R. B. Tully and J. R. Fisher, “Reprint of 1977A&A....54..661T. A new method of determining distance to galaxies.,” , vol. 500, pp. 105–117, Feb. 1977.
- [57] S. Torres-Flores, B. Epinat, P. Amram, H. Plana, and C. Mendes de Oliveira, “GHASP: an H α kinematic survey of spiral and irregular galaxies - IX. The near-infrared, stellar and baryonic Tully-Fisher relations,” , vol. 416, pp. 1936–1948, Sept. 2011.
- [58] B. K. Moorthy and J. A. Holtzman, “Stellar populations in bulges of spiral galaxies,” , vol. 371, pp. 583–608, Sep 2006.
- [59] D. A. Gadotti, “Structural properties of pseudo-bulges, classical bulges and elliptical galaxies: a Sloan Digital Sky Survey perspective,” , vol. 393, pp. 1531–1552, Mar 2009.
- [60] J. Kormendy and J. Kennicutt, Robert C., “Secular Evolution and the Formation of Pseudobulges in Disk Galaxies,” , vol. 42, pp. 603–683, Sep 2004.
- [61] D. B. Fisher and N. Drory, “The Structure of Classical Bulges and Pseudobulges: the Link Between Pseudobulges and SÉRSIC Index,” , vol. 136, pp. 773–839, Aug 2008.
- [62] K. Ganda, J. Falcón-Barroso, R. F. Peletier, M. Cappellari, E. Emsellem, R. M. McDermid, P. Tim de Zeeuw, and C. M. Carollo, “Late-type galaxies observed with SAURON: two-dimensional stellar and emission-line kinematics of 18 spi-

rals,” *Monthly Notices of the Royal Astronomical Society*, vol. 367, pp. 46–78, 03 2006.

- [63] L. F. Whyte, R. G. Abraham, M. R. Merrifield, P. B. Eskridge, J. A. Frogel, and R. W. Pogge, “Morphological classification of the OSU Bright Spiral Galaxy Survey,” , vol. 336, pp. 1281–1286, Nov 2002.
- [64] F. Combes and R. H. Sanders, “Formation and properties of persisting stellar bars.,” , vol. 96, pp. 164–173, Mar 1981.
- [65] L. C. Ho, A. V. Filippenko, and W. L. W. Sargent, *Low-Luminosity Seyfert Nuclei.*, vol. 113 of *Astronomical Society of the Pacific Conference Series*, p. 429. 1997.
- [66] R. A. Benjamin, *The Spiral Structure of the Galaxy: Something Old, Something New...*, vol. 387 of *Astronomical Society of the Pacific Conference Series*, p. 375. 2008.
- [67] J. S. Young and N. Z. Scoville, “Molecular gas in galaxies.,” , vol. 29, pp. 581–625, Jan. 1991.
- [68] M. Obrić, Ž. Ivezić, P. N. Best, R. H. Lupton, C. Tremonti, J. Brinchmann, M. A. Agüeros, G. R. Knapp, J. E. Gunn, C. M. Rockosi, D. Schlegel, D. Finkbeiner, M. Gaćesa, V. Smolčić, S. F. Anderson, W. Voges, M. Jurić, R. J. Siverd, W. Steinhardt, A. S. Jagoda, M. R. Blanton, and D. P. Schneider, “Panchromatic properties of 99000 galaxies detected by SDSS, and (some by) ROSAT, GALEX, 2MASS, IRAS, GB6, FIRST, NVSS and WENSS surveys,” , vol. 370, pp. 1677–1698, Aug. 2006.
- [69] A. N. Witt and K. D. Gordon, “Multiple Scattering in Clumpy Media. II. Galactic Environments,” , vol. 528, pp. 799–816, Jan. 2000.

- [70] A. H. Maller, A. A. Berlind, M. R. Blanton, and D. W. Hogg, “The Intrinsic Properties of SDSS Galaxies,” , vol. 691, pp. 394–406, Jan. 2009.
- [71] R. D. Propris, C. J. Conselice, J. Liske, S. P. Driver, D. R. Patton, A. W. Graham, and P. D. Allen, “The millennium galaxy catalogue: The connection between close pairs and asymmetry implications for the galaxy merger rate,” *The Astrophysical Journal*, vol. 666, pp. 212–221, sep 2007.
- [72] E. J. Barton, M. J. Geller, and S. J. Kenyon, “Tidally Triggered Star Formation in Close Pairs of Galaxies,” , vol. 530, pp. 660–679, Feb. 2000.
- [73] T. J. Cox, P. Jonsson, J. R. Primack, and R. S. Somerville, “Feedback in simulations of disc-galaxy major mergers,” , vol. 373, pp. 1013–1038, Dec. 2006.
- [74] D. B. Sanders and I. F. Mirabel, “Luminous infrared galaxies,” *Annual Review of Astronomy and Astrophysics*, vol. 34, no. 1, pp. 749–792, 1996.
- [75] A. I. Zabludoff, D. Zaritsky, H. Lin, D. Tucker, Y. Hashimoto, S. A. Shectman, A. Oemler, and R. P. Kirshner, “The Environment of “E+A” Galaxies,” , vol. 466, p. 104, July 1996.
- [76] L. Ferrarese and D. Merritt, “A Fundamental Relation between Supermassive Black Holes and Their Host Galaxies,” , vol. 539, pp. L9–L12, Aug 2000.
- [77] G. Kauffmann and M. Haehnelt, “A unified model for the evolution of galaxies and quasars,” , vol. 311, pp. 576–588, Jan 2000.
- [78] B. Catinella, A. Saintonge, S. Janowiecki, L. Cortese, R. Davé, J. J. Lemonias, A. P. Cooper, D. Schiminovich, C. B. Hummels, S. Fabello, K. Geréb, V. Kilborn, and J. Wang, “xGASS: total cold gas scaling relations and molecular-to-atomic gas ratios of galaxies in the local Universe,” , vol. 476, pp. 875–895, May 2018.

- [79] I. Lamperti, A. Saintonge, I. De Looze, G. Accurso, C. J. R. Clark, M. W. L. Smith, C. D. Wilson, E. Brinks, T. Brown, M. Bureau, D. L. Clements, S. Eales, D. H. W. Glass, H. S. Hwang, J. C. Lee, L. Lin, M. J. Michalowski, M. Sargent, T. G. Williams, T. Xiao, and C. Yang, “JINGLE - V. Dust properties of nearby galaxies derived from hierarchical Bayesian SED fitting,” , vol. 489, pp. 4389–4417, Nov. 2019.
- [80] D. Foreman-Mackey, D. W. Hogg, D. Lang, and J. Goodman, “emcee: The MCMC Hammer,” , vol. 125, p. 306, Mar 2013.
- [81] D. Foreman-Mackey, “Fitting a plane to data by dan foreman-mackey,” Jun 2017.
- [82] C. P. Robert and G. Casella, *Monte Carlo Statistical Methods (Springer Texts in Statistics)*. Berlin, Heidelberg: Springer-Verlag, 2005.
- [83] A. Saintonge, G. Kauffmann, C. Kramer, L. J. Tacconi, C. Buchbender, B. Catinella, S. Fabello, J. Graciá-Carpio, J. Wang, L. Cortese, J. Fu, R. Genzel, R. Giovanelli, Q. Guo, M. P. Haynes, T. M. Heckman, M. R. Krumholz, J. Lemorias, C. Li, S. Moran, N. Rodriguez-Fernandez, D. Schiminovich, K. Schuster, and A. Sievers, “COLD GASS, an IRAM legacy survey of molecular gas in massive galaxies - I. Relations between H₂, H I, stellar content and structural properties,” , vol. 415, pp. 32–60, July 2011.
- [84] K. E. Whitaker, P. G. van Dokkum, G. Brammer, and M. Franx, “The Star Formation Mass Sequence Out to z = 2.5,” , vol. 754, p. L29, Aug. 2012.
- [85] G. Accurso, A. Saintonge, B. Catinella, L. Cortese, R. Davé, S. H. Dunsheath, R. Genzel, J. Gracia-Carpio, T. M. Heckman, Jimmy, C. Kramer, C. Li, K. Lutz, D. Schiminovich, K. Schuster, A. Sternberg, E. Sturm, L. J. Tacconi, K. V. Tran, and J. Wang, “Deriving a multivariate α_{CO} conversion function using the

[C II]/CO (1-0) ratio and its application to molecular gas scaling relations,” , vol. 470, pp. 4750–4766, Oct. 2017.

- [86] M. W. L. Smith, C. J. R. Clark, I. De Looze, I. Lamperti, A. Saintonge, C. D. Wilson, G. Accurso, E. Brinks, M. Bureau, E. J. Chung, P. J. Cigan, D. L. Clements, T. Dharmawardena, L. Fanciullo, Y. Gao, Y. Gao, W. K. Gear, H. L. Gomez, J. Greenslade, H. S. Hwang, F. Kemper, J. C. Lee, C. Li, L. Lin, L. Liu, D. C. Molnár, A. Mok, H.-A. Pan, M. Sargent, P. Scicluna, C. M. A. Smith, S. Urquhart, T. G. Williams, T. Xiao, C. Yang, and M. Zhu, “JINGLE, a JCMT legacy survey of dust and gas for galaxy evolution studies: II. SCUBA-2 850 μ m data reduction and dust flux density catalogues,” , vol. 486, pp. 4166–4185, July 2019.
- [87] K. D. Gordon, J. Roman-Duval, C. Bot, M. Meixner, B. Babler, J.-P. Bernard, A. Bolatto, M. L. Boyer, G. C. Clayton, C. Engelbracht, Y. Fukui, M. Galametz, F. Galliano, S. Hony, A. Hughes, R. Indebetouw, F. P. Israel, K. Jameson, A. Kawamura, V. Lebouteiller, A. Li, S. C. Madden, M. Matsuura, K. Misselt, E. Montiel, K. Okumura, T. Onishi, P. Panuzzo, D. Paradis, M. Rubio, K. Sandstrom, M. Sauvage, J. Seale, M. Sewiło, K. Tchernyshyov, and R. Skibba, “Dust and Gas in the Magellanic Clouds from the HERITAGE Herschel Key Project. I. Dust Properties and Insights into the Origin of the Submillimeter Excess Emission,” , vol. 797, p. 85, Dec. 2014.
- [88] A. Coupeaud, K. Demyk, C. Meny, C. Nayral, F. Delpech, H. Leroux, C. Depecker, G. Creff, J. B. Brubach, and P. Roy, “Low-temperature FIR and submillimetre mass absorption coefficient of interstellar silicate dust analogues,” , vol. 535, p. A124, Nov. 2011.
- [89] K. N. Abazajian, J. K. Adelman-McCarthy, M. A. Agüeros, S. S. Allam, C. Alende Prieto, D. An, K. S. J. Anderson, S. F. Anderson, J. Annis, N. A. Bahcall,

C. A. L. Bailer-Jones, J. C. Barentine, B. A. Bassett, A. C. Becker, T. C. Beers, E. F. Bell, V. Belokurov, A. A. Berlind, E. F. Berman, M. Bernardi, S. J. Bickerton, D. Bizyaev, J. P. Blakeslee, M. R. Blanton, J. J. Bochanski, W. N. Boroski, H. J. Brewington, J. Brinchmann, J. Brinkmann, R. J. Brunner, T. Budavári, L. N. Carey, S. Carliles, M. A. Carr, F. J. Castander, D. Cinabro, A. J. Connolly, I. Csabai, C. E. Cunha, P. C. Czarapata, J. R. A. Davenport, E. de Haas, B. Dilday, M. Doi, D. J. Eisenstein, M. L. Evans, N. W. Evans, X. Fan, S. D. Friedman, J. A. Frieman, M. Fukugita, B. T. Gänsicke, E. Gates, B. Gillespie, G. Gilmore, B. Gonzalez, C. F. Gonzalez, E. K. Grebel, J. E. Gunn, Z. Györy, P. B. Hall, P. Harding, F. H. Harris, M. Harvanek, S. L. Hawley, J. J. E. Hayes, T. M. Heckman, J. S. Hendry, G. S. Hennessy, R. B. Hindsley, J. Hoblitt, C. J. Hogan, D. W. Hogg, J. A. Holtzman, J. B. Hyde, S.-i. Ichikawa, T. Ichikawa, M. Im, Ž. Ivezić, S. Jester, L. Jiang, J. A. Johnson, A. M. Jorgensen, M. Jurić, S. M. Kent, R. Kessler, S. J. Kleinman, G. R. Knapp, K. Konishi, R. G. Kron, J. Krzesinski, N. Kuropatkin, H. Lampeitl, S. Lebedeva, M. G. Lee, Y. S. Lee, R. French Leger, S. Lépine, N. Li, M. Lima, H. Lin, D. C. Long, C. P. Loomis, J. Loveday, R. H. Lupton, E. Magnier, O. Malanushenko, V. Malanushenko, R. Mandelbaum, B. Margon, J. P. Marriner, D. Martínez-Delgado, T. Matsubara, P. M. McGehee, T. A. McKay, A. Meiksin, H. L. Morrison, F. Mullally, J. A. Munn, T. Murphy, T. Nash, A. Nebot, J. Neilsen, Eric H., H. J. Newberg, P. R. Newman, R. C. Nichol, T. Nicinski, M. Nieto-Santisteban, A. Nitta, S. Okamura, D. J. Oravetz, J. P. Ostriker, R. Owen, N. Padmanabhan, K. Pan, C. Park, G. Pauls, J. Peoples, John, W. J. Percival, J. R. Pier, A. C. Pope, D. Pourbaix, P. A. Price, N. Purger, T. Quinn, M. J. Raddick, P. Re Fiorentin, G. T. Richards, M. W. Richmond, A. G. Riess, H.-W. Rix, C. M. Rockosi, M. Sako, D. J. Schlegel, D. P. Schneider, R.-D. Scholz, M. R. Schreiber, A. D. Schwone, U. Seljak, B. Sesar, E. Sheldon, K. Shimasaku, V. C. Sibley, A. E.

Simmons, T. Sivarani, J. Allyn Smith, M. C. Smith, V. Smolčić, S. A. Snedden, A. Stebbins, M. Steinmetz, C. Stoughton, M. A. Strauss, M. SubbaRao, Y. Suto, A. S. Szalay, I. Szapudi, P. Szkody, M. Tanaka, M. Tegmark, L. F. A. Teodoro, A. R. Thakar, C. A. Tremonti, D. L. Tucker, A. Uomoto, D. E. Vanden Berk, J. Vandenberg, S. Vidrih, M. S. Vogeley, W. Voges, N. P. Vogt, Y. Wadadekar, S. Watters, D. H. Weinberg, A. A. West, S. D. M. White, B. C. Wilhite, A. C. Wonders, B. Yanny, D. R. Yocom, D. G. York, I. Zehavi, S. Zibetti, and D. B. Zucker, “The Seventh Data Release of the Sloan Digital Sky Survey,” , vol. 182, pp. 543–558, June 2009.

- [90] S. Salim, R. M. Rich, S. Charlot, J. Brinchmann, B. D. Johnson, D. Schiminovich, M. Seibert, R. Mallory, T. M. Heckman, K. Forster, P. G. Friedman, D. C. Martin, P. Morrissey, S. G. Neff, T. Small, T. K. Wyder, L. Bianchi, J. Donas, Y.-W. Lee, B. F. Madore, B. Milliard, A. S. Szalay, B. Y. Welsh, and S. K. Yi, “UV Star Formation Rates in the Local Universe,” , vol. 173, pp. 267–292, Dec. 2007.
- [91] J. Brinchmann, S. Charlot, S. D. M. White, C. Tremonti, G. Kauffmann, T. Heckman, and J. Brinkmann, “The physical properties of star-forming galaxies in the low-redshift Universe,” , vol. 351, pp. 1151–1179, July 2004.
- [92] T. Jones, D. P. Stark, and R. S. Ellis, “Dust in the Wind: Composition and Kinematics of Galaxy Outflows at the Peak Epoch of Star Formation,” , vol. 863, p. 191, Aug. 2018.
- [93] M. G. Jones, M. P. Haynes, R. Giovanelli, and C. Moorman, “The ALFALFA H I mass function: a dichotomy in the low-mass slope and a locally suppressed ‘knee’ mass,” , vol. 477, pp. 2–17, June 2018.
- [94] T. J. Fletcher, A. Saintonge, P. S. Soares, and A. Pontzen, “The cosmic abundance of neutral hydrogen in the local universe,” , vol. 477, pp. 18–32, June 2018.

dance of cold gas in the local Universe," *arXiv e-prints*, p. arXiv:2002.04959, Feb. 2020.

- [95] H.-A. Pan, L. Lin, B.-C. Hsieh, S. F. Sánchez, H. Ibarra-Medel, M. Boquien, I. Lacerna, M. Argudo-Fernández, D. Bizyaev, M. Cano-Díaz, N. Drory, Y. Gao, K. Masters, K. Pan, M. Tabor, P. Tissera, and T. Xiao, "SDSS IV MaNGA: Dependence of Global and Spatially Resolved SFR- M_* Relations on Galaxy Properties," , vol. 854, p. 159, Feb. 2018.
- [96] DESI Collaboration, A. Aghamousa, J. Aguilar, S. Ahlen, S. Alam, L. E. Allen, C. Allende Prieto, J. Annis, S. Bailey, C. Balland, O. Ballester, C. Baltay, L. Beaufore, C. Bebek, T. C. Beers, E. F. Bell, J. L. Bernal, R. Besuner, F. Beutler, C. Blake, H. Bleuler, M. Blomqvist, R. Blum, A. S. Bolton, C. Briceno, D. Brooks, J. R. Brownstein, E. Buckley-Geer, A. Burden, E. Burtin, N. G. Busca, R. N. Cahn, Y.-C. Cai, L. Cardiel-Sas, R. G. Carlberg, P.-H. Carton, R. Casas, F. J. Castander, J. L. Cervantes-Cota, T. M. Claybaugh, M. Close, C. T. Coker, S. Cole, J. Comparat, A. P. Cooper, M. C. Cousinou, M. Crocce, J.-G. Cuby, D. P. Cunningham, T. M. Davis, K. S. Dawson, A. de la Macorra, J. De Vicente, T. Delubac, M. Derwent, A. Dey, G. Dhungana, Z. Ding, P. Doel, Y. T. Duan, A. Ealet, J. Edelstein, S. Eftekharzadeh, D. J. Eisenstein, A. Elliott, S. Escoffier, M. Evatt, P. Fagrelius, X. Fan, K. Fanning, A. Farahi, J. Farahi, G. Favole, Y. Feng, E. Fernandez, J. R. Findlay, D. P. Finkbeiner, M. J. Fitzpatrick, B. Flaugher, S. Flender, A. Font-Ribera, J. E. Forero-Romero, P. Fosalba, C. S. Frenk, M. Fumagalli, B. T. Gaensicke, G. Gallo, J. Garcia-Bellido, E. Gaztanaga, N. Pietro Gentile Fusillo, T. Gerard, I. Gershkovich, T. Giannantonio, D. Gillet, G. Gonzalez-de-Rivera, V. Gonzalez-Perez, S. Gott, O. Graur, G. Gutierrez, J. Guy, S. Habib, H. Heetderks, I. Heetderks, K. Heitmann, W. A. Hellwing, D. A. Herrera, S. Ho, S. Holland, K. Honscheid, E. Huff,

T. A. Hutchinson, D. Huterer, H. S. Hwang, J. M. Illa Laguna, Y. Ishikawa, D. Jacobs, N. Jeffrey, P. Jelinsky, E. Jennings, L. Jiang, J. Jimenez, J. Johnson, R. Joyce, E. Jullo, S. Juneau, S. Kama, A. Karcher, S. Karkar, R. Kehoe, N. Kennamer, S. Kent, M. Kilbinger, A. G. Kim, D. Kirkby, T. Kisner, E. Kitaniidis, J.-P. Kneib, S. Koposov, E. Kovacs, K. Koyama, A. Kremin, R. Kron, L. Kronig, A. Kueter-Young, C. G. Lacey, R. Lafever, O. Lahav, A. Lambert, M. Lampton, M. Land riau, D. Lang, T. R. Lauer, J.-M. Le Goff, L. Le Guillou, A. Le Van Suu, J. H. Lee, S.-J. Lee, D. Leitner, M. Lesser, M. E. Levi, B. L'Huillier, B. Li, M. Liang, H. Lin, E. Linder, S. R. Loebman, Z. Lukić, J. Ma, N. MacCrann, C. Magneville, L. Makarem, M. Manera, C. J. Manser, R. Marshall, P. Martini, R. Massey, T. Matheson, J. McCauley, P. McDonald, I. D. McGreer, A. Meisner, N. Metcalfe, T. N. Miller, R. Miquel, J. Moustakas, A. Myers, M. Naik, J. A. Newman, R. C. Nichol, A. Nicola, L. Nicolati da Costa, J. Nie, G. Niz, P. Norberg, B. Nord, D. Norman, P. Nugent, T. O'Brien, M. Oh, K. A. G. Olsen, C. Padilla, H. Padmanabhan, N. Padmanabhan, N. Palanque-Delabrouille, A. Palmese, D. Pappalardo, I. Pâris, C. Park, A. Patej, J. A. Peacock, H. V. Peiris, X. Peng, W. J. Percival, S. Perruchot, M. M. Pieri, R. Pogge, J. E. Pollack, C. Poppett, F. Prada, A. Prakash, R. G. Probst, D. Rabinowitz, A. Raichoor, C. H. Ree, A. Refregier, X. Regal, B. Reid, K. Reil, M. Rezaie, C. M. Rockosi, N. Roe, S. Ronayette, A. Roodman, A. J. Ross, N. P. Ross, G. Rossi, E. Rozo, V. Ruhlmann-Kleider, E. S. Rykoff, C. Sabiu, L. Samushia, E. Sanchez, J. Sanchez, D. J. Schlegel, M. Schneider, M. Schubnell, A. Secroun, U. Seljak, H.-J. Seo, S. Serrano, A. Shafieloo, H. Shan, R. Sharples, M. J. Sholl, W. V. Shourt, J. H. Silber, D. R. Silva, M. M. Sirk, A. Slosar, A. Smith, G. F. Smoot, D. Som, Y.-S. Song, D. Sprayberry, R. Staten, A. Stefanik, G. Tarle, S. Sien Tie, J. L. Tinker, R. Tojeiro, F. Valdes, O. Valenzuela, M. Valluri, M. Vargas-Magana, L. Verde, A. R. Walker, J. Wang, Y. Wang, B. A. Weaver,

C. Weaverdyck, R. H. Wechsler, D. H. Weinberg, M. White, Q. Yang, C. Yeh, T. Zhang, G.-B. Zhao, Y. Zheng, X. Zhou, Z. Zhou, Y. Zhu, H. Zou, and Y. Zu, “The DESI Experiment Part I: Science, Targeting, and Survey Design,” *arXiv e-prints*, p. arXiv:1611.00036, Oct. 2016.

- [97] W. J. Percival, L. Samushia, A. J. Ross, C. Shapiro, and A. Raccanelli, “Redshift-space distortions,” *Philosophical Transactions of the Royal Society of London Series A*, vol. 369, pp. 5058–5067, Dec. 2011.